ORIGINAL ARTICLE

Application of processing maps and numerical modelling for identification of parameters and limitations of hot forging process of 80MnSi8-6 steel

Marek Wojtaszek[1] · Łukasz Lisiecki[1] · Aneta Łukaszek-Sołek[1] · Grzegorz Korpała[3] · Krystian Zyguła[1] ·
Tomasz Śleboda[1] · Magdalena Barbara Jabłońska[2] · Ulrich Prahl[3]

Abstract

The processing maps developed by dynamic material modelling (DMM) method are now widely used in the design of hot forming processes. However, this applies to those processes that are relatively fast or are carried out under isothermal conditions, when it is possible to maintain the deformation parameters within the processing window. In the case of multi-stage free forging, the temperature successively decreases during subsequent operations and is increased during inter-process reheating. Under such conditions, processing maps in direct form are not applicable. The proposed solution is to implement the data obtained by the DMM method into calculations carried out by the finite element method (FEM). This approach leads to obtain the distributions of DMM parameters in the volume of the feedstock at successive forging stages. Selected results of a combined DMM/FEM analysis of a multi-stage hot forging process of 80MnSi8-6 steel are presented. The starting data for the analysis were the flow curves of this material, determined from compression tests. The processing maps were developed and processing windows were determined. The results of the DMM analysis were verified by microstructure observations. Data from the DMM analysis were implemented into QForm software using LUA scripts. An integrated FEM/DMM numerical analysis of the process of a multi-step hot free forging of an example product was performed. The geometry of the tools and a sequence of operations were developed. The distributions of the DMM parameters and the hot deformation activation energy in the forging volume after successive forging sequences were analyzed.

1 Introduction

Bainite is an aggregate of phases, consisting of plates of ferrite doped with minority phases such as carbides or residual austenite [1]. This microstructure can be generated throughout the component or in zones near the surface to improve tribological properties [2]. Recent research has shown that the comparison of the mechanical properties of bainitic steels with the properties of conventional steels is promising [3]. It was also noticed that the properties of this type of steel depend on the size of the phase components. A typical bainite contains bainitic ferrite with a thickness of about 0.2–0.5 μm and an average length of about 100 μm [4]. However, the size of bainite can be adjusted from tens of nanometres to hundreds of micrometers [5]. By varying the scale of the microstructure, the properties of the products can be controlled. Nanostructured microstructures, consisting of a mixture of very thin plates of bainitic ferrite separated by carbon-enriched austenite, are the characteristics of the so-called nanobain steel group [6]. To this day, nanobain steels are the subject of intensive research aimed at improving their microstructure. For example, Królicka et al. [7] demonstrated that both qualitative and quantitative analyzes play

✉ Marek Wojtaszek
  wojtaszek@agh.edu.pl

1 Faculty of Metals Engineering and Industrial Computer Science, AGH University of Science and Technology, Al. A. Mickiewicza 30, 30-059 Kraków, Poland

2 Faculty of Materials Engineering, Silesian University of Technology, Krasińskiego 8, 40-019 Katowice, Poland

3 Institut für Metallformung, TU Bergakademie Freiberg, Bernhard-von-Cotta-Straße 4, 09599 Freiberg, Germany

a key role in the microstructural characterization of nanobainitic steels, with particular emphasis on their mechanical properties. Bainite is an aggregate of phases, consisting of plates of ferrite doped with minority phases such as carbides or residual [8], compared to many high-performance steels [9]. The presence of this type of microstructure is also associated with resistance to abrasive wear [10], as demonstrated in tests by Rios-Diez et al. Rios-Diez et al. [11] and Du Y et al. [12]. Recent studies have shown that the combination of the mentioned properties allows nanobain steels to be used for manufacturing unusual products, such as bullet protection armor [13].

For many years, steel has been used as one of the basic construction materials. The reason is that steel, obtained in well known, proven, and mastered technological processes, has stable physical and mechanical properties [14]. Due to the favorable combination of the properties, nanobainitic steels are suitable for the production of highly responsible structural components with high weights. This type of product is produced using hot free forging processes, after which the forgings are cooled in air. The next stage is the heat treatment necessary to obtain the desired microstructure. The main limitation of this technology is that the hardening of large-sized forgings to obtain a uniform bainite microstructure takes several days, making the process currently economically unjustifiable. Additionally, the heat treatment facilities used in industry are designed to handle treatments of 2–4 h, but not for 20 h or more [15]. As nanobain steels are now seen as materials with significant application potential, an analysis of the literature allows to identify the main directions to be taken into account when designing these alloys and the technology for manufacturing products from them. The first is the development of a multi-step hot forging process in such a way that, at the end of the process, a favorable initial microstructure for heat treatment is obtained. The second is the economic aspect of reducing the price of the alloy and the heat treatment time required to obtain the nanobainite microstructure, which currently takes several days.

Due to economic considerations, it is assumed that nanobain steels must be cost-effective in production, which can be achieved by excluding expensive elements such as cobalt and nickel from their chemical composition. For this reason, researchers have focused on developing compositions using relatively inexpensive elements like Fe-C-Si-Mn-Cr. Efforts aimed at reducing component costs have been pursued, including by Garcia-Mateo et al. [16]. Technological solutions are required at present, providing a reduction in energy consumption [17]. Therefore, the next direction involves efforts to significantly shorten the time of isothermal heat treatment that leads to transformation. Bainite subunits thinner than 100 nm are often achieved by conducting heat treatments in the temperature range of 200–400 °C [4].

The initial experimental work devoted to designing nanobain steel aimed to achieve nanobainite at the lowest possible temperature. For this purpose, the chemical composition was tailored to enable bainitic transformation at temperatures below 200 °C. An example is the nanobain steel with the chemical composition Fe-0.78C-1.59Si-1.94Mn-1.33Cr-0.30Mo-0.02Ni-0.11 V (wt-%), developed by Caballero et al. [18], which was obtained through heat treatment at around 125 °C. The addition of approximately 2% silicon by weight to the steel enabled the formation of a characteristic microstructure, consisting of a mixture of bainitic ferrite, carbon-enriched residual austenite, and some martensite. However, at such temperatures, the transformation required over 2 months and around 10 days at 200 °C. The advancement of research on these materials has led to a significant reduction in this time; even finer bainitic microstructures were achieved at 200 °C in just 3 days [6]. An example was a steel with the chemical composition Fe-0.83C-1.57Si-1.98Mn-1.02Cr-0.24Mo-1.54Co-0.11 V. The proposed improvement was based on two concepts, involving controlling the austenitization conditions before bainitic transformation and introducing approximately 1.5% mass of relatively expensive cobalt into the chemical composition. This approach accelerated the transformation kinetics. As a result, materials were obtained that exhibited a very good combination of yield strength, ultimate tensile strength, ductility, and respectable levels of fracture [19]. In works related to nanobain steels, conducted by Garcia-Mateo et al. [16], economic aspects were also taken into account. The aim was to obtain nanostructured bainitic steels through transformation at low temperatures within an industrially acceptable timeframe and using cost-effective alloying additions. Another example of a material that, under carefully developed conditions, can meet these criteria is the 80MnSi8-6 steel.

The nanobain steels can be free-forged not only into large-scale products but also into small series of structural elements such as crankshafts, rolls, rings, or sleeves with smaller dimensions. This applies especially to structural components intended to operate in conditions where wear is the main damage mechanism. Nanobainitic steels have tremendous potential as materials for producing such products [20]. A limitation of the open-die forging technology is the need for a series of forging and heating operations, which require a correspondingly long time. This time depends mainly on the adopted degree of forging and the final shape of the forged piece. As a result, intermittent re-heating is often necessary, which is costly, time-consuming, and leads to grain growth. This is particularly relevant for relatively small forgings, ranging from a few to several tens of kilograms, which quickly dissipate heat to the surroundings and to the tools. Therefore, the manufacturing technology for such products needs to be designed to minimize the number of heat treatment steps

to the necessary minimum. Another key requirement for achieving nanobainite is to ensure the appropriate initial microstructure in the hot forging process. Hence, the process must be conducted in a way that ensures a homogeneous microstructure and the smallest possible grain size. As a result, designing the steps of multi-stage forging for nanobainitic steel products requires advanced knowledge of material behavior in relation to thermo-mechanical deformation parameters. One of the approaches used to develop such knowledge is the dynamic material modeling (DMM) method.

During hot forming of metals and alloys, changes in microstructure occur alongside shape changes, which significantly influence the properties of the final product. These changes are primarily associated with the occurrence of dynamic recovery (DRV) and dynamic recrystallisation (DRX) mechanisms [21] or phase transformations [22]. In recent years, the DMM method has been employed to analyze the behavior of many structural materials during plastic deformation. The essence of this method lies in defining the material as an energy dissipation field and determining its ability to dissipate the portion of energy that leads to microstructural changes during deformation. This method requires knowledge of the material's stress–strain curves. It involves deducing changes in the sensitivity parameter of flow stress to the strain rate m based on these curves and developing deformation efficiency maps [22]. These maps are often supplemented by instability maps, constructed using the flow instability parameter ξ. This parameter identifies combinations of temperatures and strain rates that can induce microstructural flow instabilities [23]. In practice, within regions indicated as potentially unstable, the microstructure inside the material is improved, if the power dissipation value is high [24], which resulting in enhanced formability [25]. Combining deformation efficiency maps with instability maps leads to the development of so-called processing maps. This approach leads to obtain the tool that is valuable for analyzing material behavior within a selected range of temperature and strain rate. This is a universal tool, as thermomechanical processing enables obtaining final products by shaping the preforms in various processing routes [26]. For instance, in processes conducted under dynamic conditions, the deformation rate is one of parameters which may vary in a broad range, while the other parameters are constant or negligibly low [27]. On the other hand, in lengthy processes such as multi-stage forging on hydraulic presses, the material is shaped within a narrow range of strain rates, while its temperature changes significantly. Some processes, like hot rolling, involve substantial variations in temperature, strain rate, and strain value. In all these cases, processing maps can prove beneficial for analyzing material formability and designing the technology for its plastic deformation. Several criteria have been developed as the basis for DMM

calculations, with Prasad's criterion being the most commonly used nowadays [28].

Literature analysis has demonstrated that process maps developed using the DMM method are currently widely employed in the design of hot forming processes for structural elements made from various alloys, including modern steels. Chegini et al. [29] applied the DMM method to develop three-dimensional process maps for AISI 414 martensitic stainless steel. They identified four safe processing regions for hot working and showcased the significant influence of temperature and strain rate on the grain size evolution during hot deformation. Zhou et al. [30] used the DMM method to assess the hot formability of BG801 bearing steel. They indicated that unstable regions, where defects such as flow localization and microcracks occur, emerge within the microstructure when post-deformation occurs at low temperatures and relatively high strain rates. Fu et al. [31] analyzed the effect of hot deformation parameters on the microstructural state of 18Cr-5Ni-4Cu nitrogen-alloyed austenitic stainless steel using the DMM method. Hot deformation studies of 5CrNiMoV steel by Li et al. [32] using the DMM method allowed the development of critical strain and dynamic recrystallization volume fraction (DRX) models, which were constructed based on the theory of strain hardening. The results showed that the critical strain of DRX decreases with increasing strain temperature and decreasing strain rate, which means that DRX occurs easily at higher temperatures and lower strain rates. In recent years, assemblies of 3D processing maps for increasing values of true strain have been increasingly used to develop parameter ranges that are favorable during hot forming of structural components. For example, Ye et al. used this method to design a process for fabricating a Super-Large Nuclear-Power Rotor from 25Cr2Ni4MoV steel [33], while Zeng et al. developed 3D processing maps to help select shaping parameters for flat bottom cylindrical parts [34].

A novel approach to the study of formability was proposed by Chen et al. Based on the DMM method, they developed the 3D processing maps, and integrated the resulting parameter distributions with finite element method (FEM) calculations. Using Cr5 alloy steel as the test material and using the commercial program Forge [33 = 35], they determined the distribution and change of power dissipation and flow instability parameters in the volume of compression specimens using different combinations of temperature and strain rate. A similar approach was also used by Chen et al. as a tool for the analysis of hot workability of ultra-super-critical rotor steel [36].

Currently, processing maps are being used to analyze and optimize hot-forming processes. In turn, FEM can be used to simulate hot deformation processes, predict problems during production, and develop methods to reduce costs and cycle times. An example of such an approach is the work of

Hawryluk et al. in which comprehensive FEM analysis of a multistage hot-die forging on hammers, in order to improve the technology of produce a yoke-type forging [37]. Most often, DMM and FEM methods are treated as two separate analysis paths. The first emphasizes material properties, while the second focuses on comprehensive process evaluation [38]. Often the two methods are combined during process design, but not directly. This approach is implemented in two stages. The first stage involves developing processing windows using the DMM method. This is followed by an FEM analysis of processes for manufacturing specific products by hot forming, with process parameters maintained inside the designated processing windows. Examples of this approach include the work of [39]. However, this solution has its limitations. The area of application of processing maps as an effective tool for analyzing the behavior of materials during their hot plastic deformation mainly concerns those processes that last for a relatively short time, such as die forging, or are carried out under isothermal conditions. In such cases, the range of changes in the values of temperature and strain rate during the process is small enough that it is possible to maintain the values of temperature and strain rate inside processing windows throughout the process. In the case of multi-stage free forging on hydraulic presses, the strain rate does not change significantly, but the temperature successively decreases during subsequent operations. Then, if necessary, the temperature is raised to the upper limit during inter-operation reheating. As a result, the process is often conducted over the full temperature range and cannot be maintained inside the processing windows. For this reason, processing maps in direct form are not significantly applicable to the design of multi-stage free forging. The solution proposed in this paper is to transfer the data obtained by the DMM method to an FEM-based software and perform integrated simulations. This approach leads to obtaining distributions of parameters calculated by the DMM method in the volume of the forged feedstock in successive stages of its shaping.

According to the authors, understanding the relationships between thermo-mechanical deformation parameters and the values obtained through the application of the DMM method within the volume of a forging at successive stages of the hot forging process can be highly valuable in the design of multi-stage hot forging processes for steel products, including 80MnSi8-6 steel, intended for subsequent heat treatment to achieve a nanobainitic microstructure. Such an approach allows for the development of correlations between the temperature, strain rate, and strain distributions obtained through FEM modeling and their corresponding distributions of high-temperature deformation activation energy and the energy dissipation effectiveness parameter. The analysis of relevant literature revealed a limited amount of data on this topic. Chen et al. [35, 36] employed such an approach,

but they focused on FEM modeling of the thermal compression process of cylindrical specimens under various deformation conditions. A more comprehensive approach was adopted by Łukaszek-Sołek [40], who integrated DMM and FEM methods for a comprehensive analysis of the hot die forging process for selected forgings made from 4031 and 4340 steel. Even though these studies were limited to single-stage processes and short timescales, they demonstrated the significant potential of the method and how it could greatly facilitate the design of hot forging technologies. According to the authors, this particularly applies to complex and prolonged processes where using the DMM method in its conventional form is challenging due to the difficulty of maintaining parameters within process windows throughout their entire implementation. In cases where the range of deformation speeds is constrained, such as during hydraulic press forging, it becomes necessary to operate with parameters outside process windows or within potential microstructural instability regions. Modern FEM software have the capability to analyze processes conducted in multiple sequential steps. For example, current capabilities of software like QForm include modeling FEM processes performed in multiple sequences, tool exchange, interoperative rotation and movement of billets, interoperative reheating, and other advanced features. However, despite these capabilities, apart from a few publications related to compression or hot die forging, there are limited studies that effectively combine hot processing maps with finite element methods to visualize power loss values dynamically and instability regions in different parts of forgings. This also applies to the investigated 80MnSi8-6 steel. This observation provided the motivation for conducting research, and selected results of these studies are presented in this work.

2 Experimental procedure

2.1 Examined material

The initial material for the study was the 80MnSi8-6 steel, obtained through casting processes followed by preliminary hot forging of the ingot. The chemical composition of the steel is presented in Table 1, and microstructure images in the as-received state are shown in Fig. 1.

2.2 Methods of investigation

Metallographic examination of the starting material and samples in the swollen state was performed by light microscopy, on a DM4000M microscope from Leica. The specimens were inlaid (Verso-Kit, Struers), ground (Struers abrasive films and papers), polished (MD-Chem disc, OPS suspension, diamond pastes—Struers) and etched in nital.

Table 1 Chemical composition of 80MnSi8-6 steel [wt. %]

Chemical element	C	Si	Mn	P	S	Cr	Mo	V	Fe
Content, % by mass	0.79	1.55	1.9	0.003	0.003	1.3	0.25	0.11	Bal

Fig. 1 Microstructure of 80MnSi8-6 steel

a)   b)
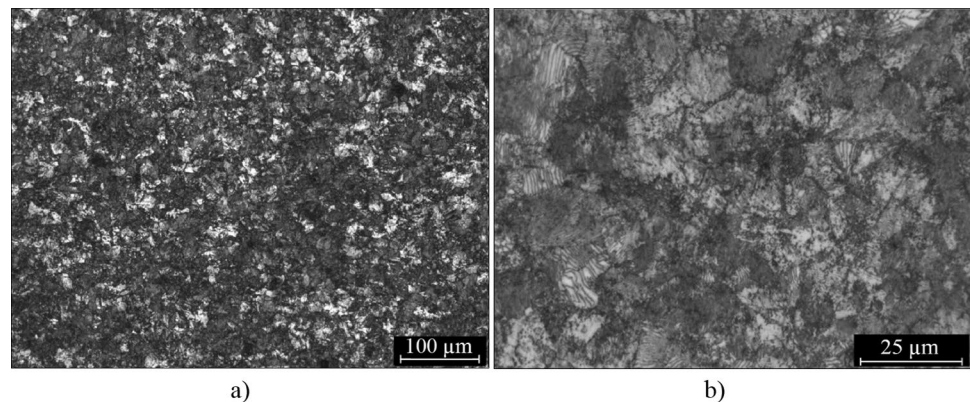
Plastometric tests were performed using a WUMSI (German: Warmumformsimulator) hydraulic hot molding simulator from BÄHR. The stand includes a system for controlling and recording test conditions and a set of furnaces. The stand allows tests of up to 400 kN loads under static conditions and up to 320 kN during tests under dynamic conditions. Heating of specimens is carried out in external furnaces. Hot compression can be carried out at a maximum test speed of 480 mm·s^{-1}, and under conditions of constant strain rate in the range of 0.01 s^{-1} do 40 s^{-1}. Samples with dimensions of ϕ 10 mm × 18 mm were placed in a heat-resistant steel container closed with a punch. The bottom of the container and the bottom of the punch were coated with graphite grease. The temperatures of the samples were controlled with a thermocouple. The tool set prepared in this way, together with the sample, was placed in an oven and heated to 1250 °C. The container was held at this temperature for 10 min, this time being sufficient to achieve the desired temperature throughout the sample volume. The container was then removed from the oven, held in the air for the time necessary to cool the sample to the test temperature, after which the hot compression was carried out at the assumed strain rate. After the test was completed, the sample was removed from the container and cooled. During deformation, temperatures of 1250, 1100, 1000 and 900 °C and strain rates of 0.1, 1, 10 and 20 s^{-1} were used, respectively.

Processing maps were developed using the Prasad criterion. It was assumed that in order to develop the data necessary to conduct integrated DMM/FEM modeling, of the hot forging process of 80MnSi8-6 steel, it is necessary to accurately trace intermediate states, corresponding to step increases in true strain. For this reason, the deformability evaluation was performed for a relatively small true strain of 0.05, then for incremental increases in true strain in the range of 0.1–1.0, using value changes in increments of 0.1, and for true strain in the range of 1.05–1.2 by adopting a value increment of 0.05. As a result, 15 processing maps were produced, which was sufficient to accurately conduct integrated numerical analysis. In the same way, maps of the distributions of the deformation activation energy Q were made. The maps and distributions of Q values for selected values of true deformation are included in this work.

Compression tests were performed on a hydraulic press with a maximum pressure of 500 T. A feedstock of 60 mm height and 30 mm diameter was used. Samples were heated in a silite furnace to 1250 °C, then cooled to the test temperature, placed on the lower tool in the working zone of the press and compression. The temperature of the feedstock was controlled with a thermocouple. Tests were conducted at 1000, 1100 i 1200 °C and at upper tool speeds of 5 and 20 mm·s^{-1}. The feedstock was compressed to a strain value of 0.5 and then cooled in the air.

Integrated numerical simulations of the multi-stage hot free forging process were carried out based on the FEM method, using the QForm 3D program. During modeling, the material was considered as an incompressible isotropic continuum. The elastic deformation range was not considered. The program performed calculations based on a rigid-viscous model with reinforcement, according to which the flow stress depends on the amount of strain, strain rate and temperature. Heat generated during deformation was included in the calculations. Levanov's first law was used to describe friction. In order to describe the rheology of the material, flow curves, developed on the basis of plastometric tests, as well as thermal characteristics of the materials determined in the range of hot plastic processing temperatures of the tested steel, were introduced into the QForm software. The sequential calculation capabilities of the

QForm program were used, including operation changes, tool changes, feedstock rotations and displacements between successive deformations, inter-operation reheating and others. DMM analysis data were implemented into QForm using LUA scripts.

3 Results

3.1 True strain–true stress curves

The true stress–strain curves developed from the compression test data of the 80MnSi8-6 steel specimens at the assumed temperatures and strain rates are summarized in Fig. 2. In order to accurately determine the actual strain during the hot compression test, corrections had to be applied, taking into account, among other things, the effects of frictional force and adiabatic heating. The necessary corrections to the curves were taken into account during standard post-processing of the compression test data. Among others,

the Hensel-Spittel method and the Siebel equation [41, 42]. Material data, such as the coefficient of friction, density, and thermal conductivity of the test material, were used to accurately determine the true flow stress during the correction process.

The flow curves show that the steel exhibits typical sensitivity to temperature and strain rate. In the initial stages of deformation, the flow stress increases rapidly, due to work hardening. This state is maintained until the peak deformation is reached, where the greatest stress is observed. With further deformation, the effects of work hardening and strain softening balance out and the stress decreases. In this step, high-temperature mechanisms such as DRV and DRX counterbalance the effects of work hardening and lead to the deformation softening phenomena. The nature of the curves changes regularly with increasing temperature, which was found for all strain rates used in the tests. For the lowest strain rate of 0.1 s^{-1} (Fig. 2a), above a strain rate of about 0.4, material flow occurs at a basically constant true strain value, regardless of the test
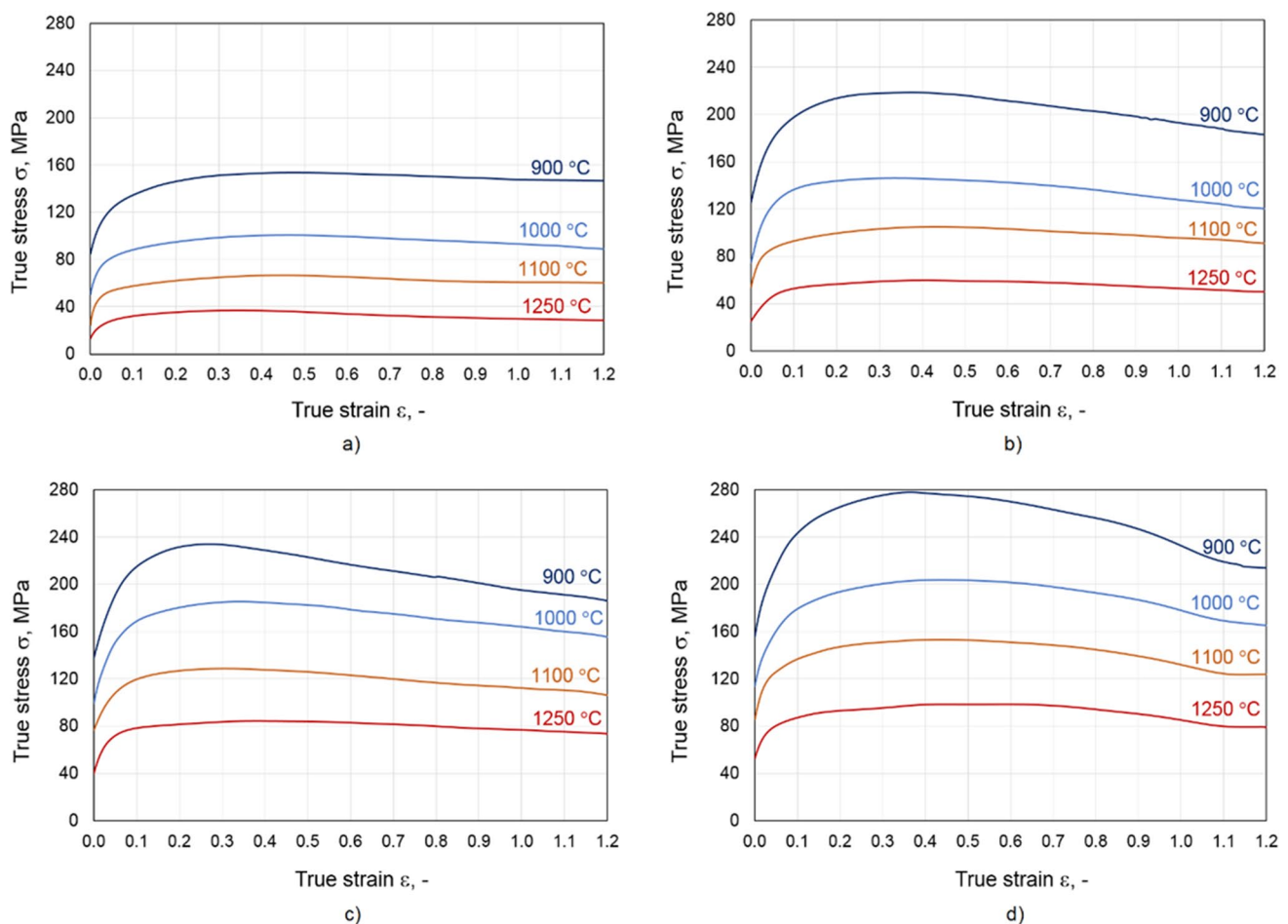

Fig. 2 Influence of thermo-mechanical parameters of realization of hot compression tests using the WUMSI simulator on the courses of flow curves of 80MnSi8-6 steel developed on their basis. Strain rate: **a** 0.1 s^{-1}, **b** 1·s^{-1}, **c** 10·s^{-1}, **d** 20·s.$^{-1}$

temperature. For higher velocities of 1 and 10-s^{-1}, there is an apparent tendency for the true stress value to decrease slightly with an increase in the value of the true strain (Fig. 2b,c). At strain rate of 20 s^{-1} (Fig. 2d), the tendency increases, and the inflection of the curve occurs at higher values of true strain, around 0.5.

3.2 Processing maps for 80MnSi8-6 steel

The processing maps in accordance with Prasad's criterion consist of a power dissipation efficiency map and flow instability map. The DMM method [22, 23] is based on the assumption that the energy absorbed by the deformed material is represented by the relation:

$$P = \sigma \cdot \dot{\varepsilon} = \int_0^{\dot{\varepsilon}} \sigma d\dot{\varepsilon} + \int_0^{\sigma} \dot{\varepsilon} d\sigma = G + J, \tag{1}$$

where:

σ_p – stress, MPa, $\dot{\varepsilon}$ – strain rate, s^{-1}, G – dissipation component representing the portion of energy that is converted to heat during plastic deformation, J – component representing the dissipation of energy due to microstructural transformations occurring during deformation.

The J component, as a function of temperature and strain rate, represents the microstructural transformations associated with DRV, DRX and phase transformations. At constant true strain, it can be expressed as follows:

$$J = \int_0^{\sigma} \dot{\varepsilon} d\sigma = \frac{\sigma \cdot \dot{\varepsilon} \cdot m}{m + 1}. \tag{2}$$

In Eq. (2), the parameter m describes the sensitivity of flow stress to strain rate and determines the relative distribution of energy (P) absorbed by the material due to heat generation (G) and as a result of microstructure remodeling (J).

The flow stress sensitivity parameter to strain rate (m) determines the relationship between heat generation (G) and microstructure changes (J) [43]. At constant true strain, this parameter is usually determined from the relationship:

$$m = \left(\frac{\partial J}{\partial G}\right)_{T,\varepsilon} = \left(\frac{\partial \log \sigma}{\partial \log \dot{\varepsilon}}\right)_{T,\varepsilon}, \tag{3}$$

where: ε – true strain, T – temperature.

The Prasad criterion was used to perform the calculations. According to this criterion, it was assumed that the energy dissipation capacity η which determines the plastic deformability of the material, is described by the relation [44]:

$$\eta = \frac{2m}{m + 1}. \tag{4}$$

Unstable flow of material during deformation can occur if the relationship is satisfied:

$$\xi = \frac{\partial \log \left(\frac{m}{m+1}\right)}{\partial \log \dot{\varepsilon}} + m < 0, \tag{5}$$

If the parameter ξ takes negative values, then microstructural flow instabilities can form in the material during deformation [22, 23]. These include flow localization, adiabatic shear bands [4], cracking [45] crystal mixing and so on [46]. Analysis of the distributions of the flow instability parameter as a function of strain rate and temperature enables the construction of instability maps. The developed map, overlaid on the energy dispersion map, forms a processing map on which processing windows can be determined. Areas where the instability parameter takes negative values are areas of potential microstructural instability. On the other hand, areas of high energy dispersion efficiency in indicate the adopted process space favorable combinations of temperature and strain rate [47].

Figure 3 shows chosen processing maps corresponding to selected constant values of true strain. They were developed by compiling the distributions of the parameter η, expressed as a percentage, and the flow instability maps (marked in navy blue the areas with negative values of the parameter ξ).

The processing map shown in Fig. 3a was developed for a low true strain of 0.05. In this range of strain, there is usually an increase in the stress value, resulting from the effect of strengthening by strain, as indicated by the flow curves (Fig. 2). In practice, this map describes the condition occurring at the initial stage of the process or at any stage of the process in areas of limited flow, such as at the metal-to-tool interface. Expressed as a percentage, the values of the η parameter range from 30 to 56% in this area, with a maximum observed at temperatures above 1100 °C and at the lowest strain rate. Overlaid on the distribution map of the η parameter, the process instability area (the area marked in navy blue), which corresponds to negative values of the ξ parameter, includes a wedge-like area. Its location in the process space covers a temperature range of 1000–1200 °C and a range of strain rates from 0.1 s^{-1} to about 6 s^{-1}.

The state corresponding to true strain 0.2 is described by the processing map shown in Fig. 3b. The highest values of the η parameter and, at the same time, the area of occurrence of negative values of the ξ parameter are
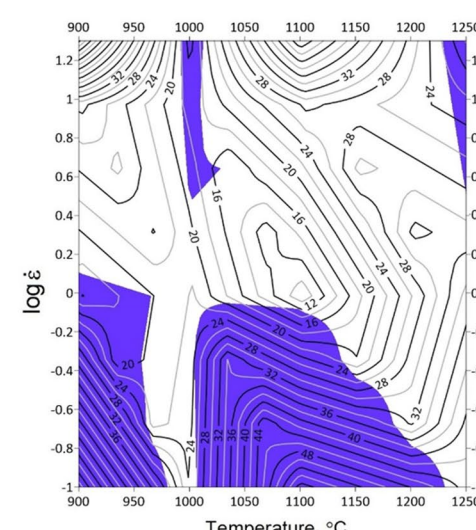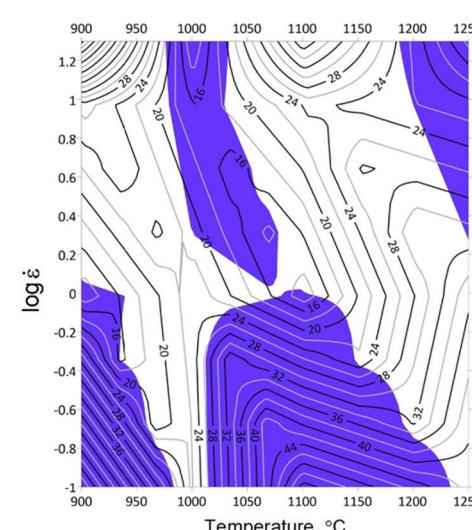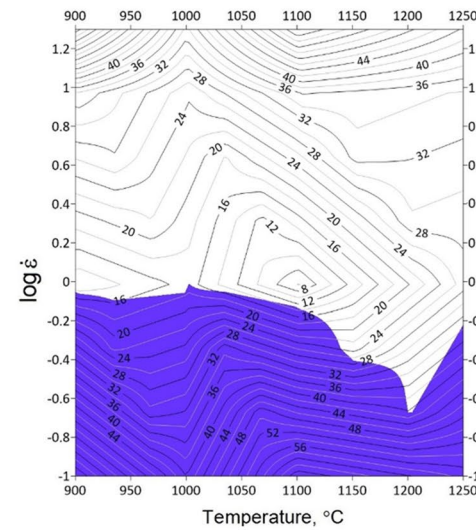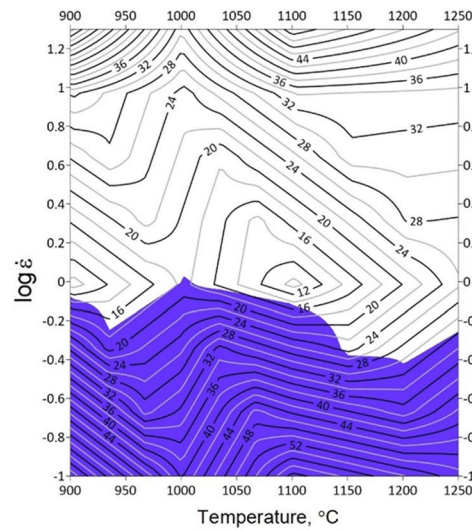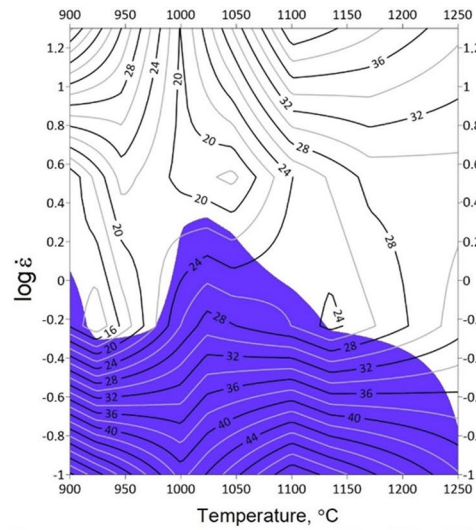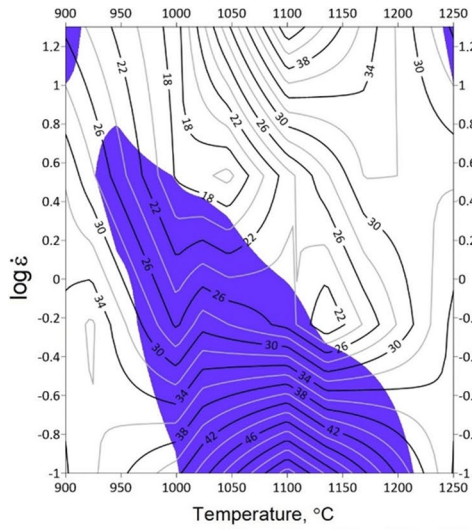
a)

b)

c)

d)

e)

f)

observed for low strain rates and over the entire temperature range. The processing maps describing the condition for true strain in the range of 0.5–0.8 are similar in nature (Fig. 3c,d). Two areas with the largest values of the η parameter are visible on them. The first occurs in a range similar to that for 0.2 deformation and covers the area of low strain rates, from $0.1\ s^{-1}$ to about $0.4\ s^{-1}$. The second area with high values of the η parameter corresponds to higher strain rates, in the range from 10 to $20\ s^{-1}$. Negative values of the ξ parameter are observed for low strain rates and over the full range of temperature.

In the processing maps developed for true strain 1.1 (Fig. 3e) and for the final value $\varepsilon = 1.2$ (Fig. 3f) respectively, the distribution of the parameter η, which expresses the ability of the material to dissipate part of the energy associated with changes in the microstructure during deformation, is smallest for the average values of strain rates, in the range from 1 to 10 s-1. This finding applies to the full temperature range. In addition, a reduced value of the η parameter over the full range of strain rates is observed in the temperature range from 975 °C to 1025 °C. In the maps developed for the true strain range from 1.1 to 1.2, four areas with negative values of the ξ parameter were identified. For higher strain rates, these areas correspond to small values of the η parameter. This combination of DMM parameters indicates unfavorable conditions for hot deformation. On the other hand, for low strain rates, zones of potential microstructural instability coincide with areas where values of the η parameter are highest. In this case, the presence of microstructural defects should be confirmed or excluded. Increasing the value of true strain from 1.1 to 1.2 does not lead to significant qualitative changes in the processing map, it only results in a narrowing of the areas with negative values of the parameter ξ in the zone of higher strain rates.

3.3 Activation energy map

To assess the deformation difficulty degree, the hot deformation activation energy Q must be taken into account. This physical parameter helps to determine the microstructure evolution and flow stress behavior during hot deformation as well as gives the opportunity to optimize the hot working processing parameters. Q is a parameter that determines the degree of difficulty in the realization of high-temperature deformation. The empirical value of energy Q for the full range of stress values, determined under conditions of constant strain value and constant strain rate, can be expressed as follows [48]:

$$Q = R \cdot n \cdot \frac{\partial \ln(\sinh(\alpha \cdot \sigma))}{\partial(1/T)}, \tag{6}$$

where: Q – the deformation activation energy (kJ/mol); T – deformation temperature (°K); σ – flow stress, (MPa); R – the universal gas constant ($8.314\ J \cdot mol^{-1} \cdot K^{-1}$); $\alpha = \beta/n_1$; α, β, n and n_1 – material constants.

The average values of the materials constants n_1, β and n at constant true strain can be calculated as:

$$n = \left[\frac{\partial ln\dot{\varepsilon}}{\partial \ln(\sinh(\alpha \cdot \sigma))} \right]_T \tag{7}$$

$$n_1 = \left(\frac{\partial ln\dot{\varepsilon}}{\partial \ln \sigma} \right)_T, \tag{8}$$

$$\beta = \left(\frac{\partial ln\dot{\varepsilon}}{\partial \sigma} \right)_T \tag{9}$$

In Table 1, the calculated material constants and values of deformation activation energy Q for 80MnSi8-6 steel were collected. Calculations were compared for selected intermediate values of true strain; 0.05, 0.2, 0.5, 0.8, 1.1, and for the final value of true strain of 1.2. Figure 4 shows examples of distribution maps of deformation activation energy Q values for the same values of true strain as selected in the set of processing maps (Fig. 3).

The value of deformation activation energy Q in the processing windows changes with increasing true strain values and as a function of temperature and strain rate (Fig. 4). For the smallest analyzed value of true strain of 0.05 (Fig. 4a), t which there is an intense effect of strengthening by crushing, the minimum of the Q value occurs in the range of strain rate $2.5\text{–}6.0\ s^{-1}$. Increasing the value of true strain shifts the area with the smallest deformation activation energy Q into the range of higher temperatures and lower strain rates (Fig. 4b). This area covers the strain rate range of 0.6–0.8, and the minimum of Q values in this area corresponds to the lowest temperature values of 900–950 °C used during testing. This condition persists in the true strain rate range up to 0.8 (Fig. 4b–d). In the energy distribution map developed for deformation 1.1 (Fig. 4e), a shift of the minimum of its value towards higher strain rates, in the range from 0.6 to 1.0, is observed. There is also an increase in the value of deformation activation energy throughout the process space. The highest value of Q is 520 kJ/mol and its position in the processing space corresponds to the range of low strain rates and high temperatures. Increasing the true strain to a final value of 1.2 (Fig. 4e) results in shifting the range of lowest Q values to the region with the highest strain rate of $20\ s^{-1}$ and the lowest temperature of 900 °C. Under these conditions, the value of Q is 385 kJ/mol. An evident trend of changes in deformation activation energy is observed,
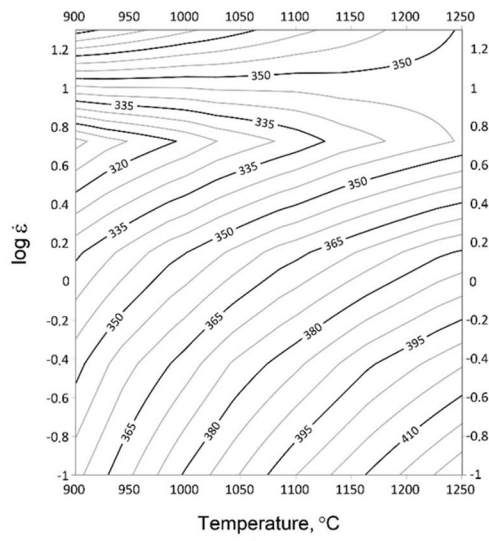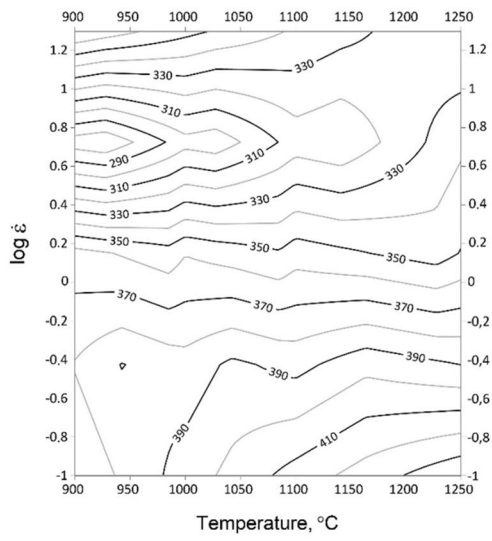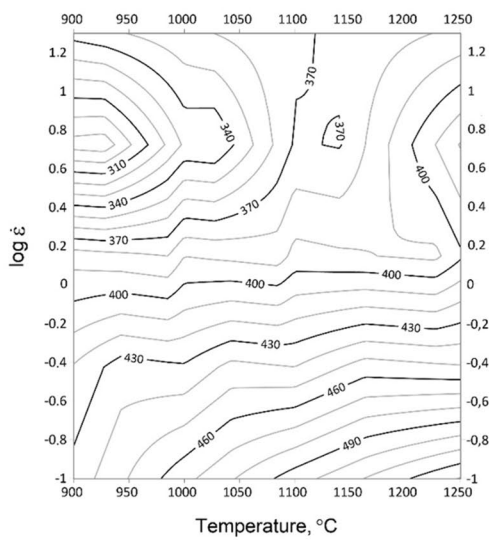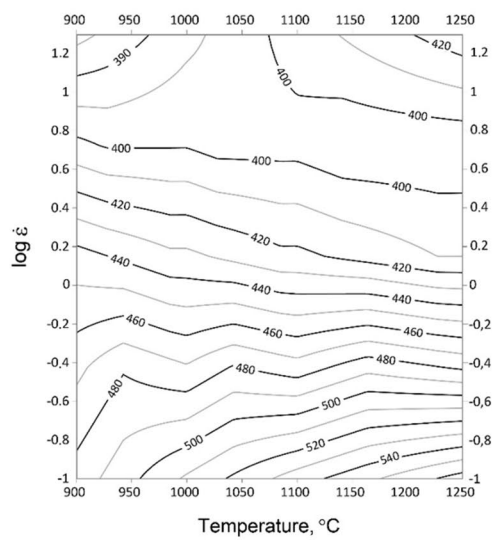
a)
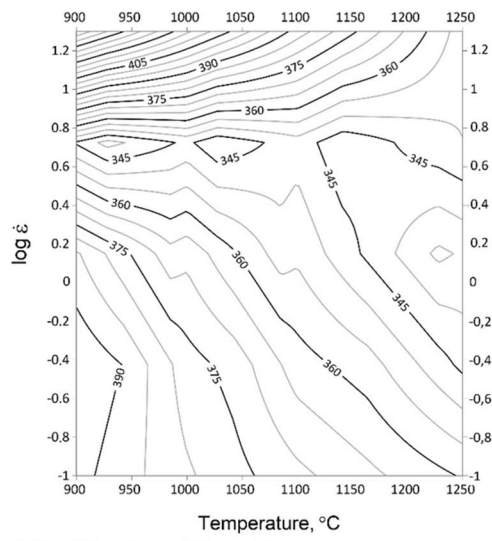
b)
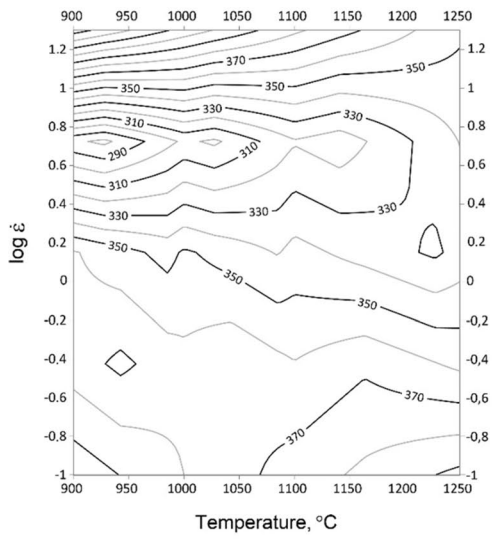
c)

d)

e)

f)

◄**Fig. 4** Selected maps of Q-value distribution in process space, developed for 80MnSi8-6 steel. Calculations for true strain values: **a** 0.05; **b** 0.2; **c** 0.5; **d** 0.8; **e** 1.1; **f** 1.2

consisting of an increase in its value as a result of increasing temperature and strain rate. As a result, the maximum $Q = 560$ kJ/mol corresponds to the superposition of a temperature of 1250 °C and a strain rate of 0.1 s-1. Changes in the average value of deformation activation energy Q in the range of true strain up to 0.8 correspond to the courses of flow curves (Fig. 3). For a low value of true strain, the average value of Q is 358 kJ/mol An increase in the value of true strain up to 0.2 leads to an increase in the value of Q, which then decreases at $\varepsilon = 0.5$ and maintains a constant value until reaching $\varepsilon = 0.8$. For high values of true strain, an increase in the average value of Q is observed, which for the final value of $\varepsilon = 1.2$ is 435 kJ/mol (Table 2).

3.4 Determination of processing windows for 80MnSi8-6 steel

The comparison of processing maps developed by the DMM method (Fig. 3a–f.) made it possible to determine in processing windows, indicating the ranges of potentially favorable combinations of shaping parameters of the material under study in hot forming processes. Figure 5a shows the location of the processing windows of 80MnSi8-6 steel. They are overlaid on a processing map developed for a true strain of 1.2, since plastometric tests were carried out until this value was reached, and microstructure observations were made for such deformed samples. Areas of potential microstructural instability are marked in navy blue, processing windows are described with numbers 1 and 2. Figure 5b shows the distribution map of energy of activation of high-temperature deformation Q corresponding to $\varepsilon = 1.2$. Figure 5 also includes an additional axis where the values of the strain rates at which the tests were performed on the WUMSI simulator are plotted.

For high strain rates, in the range of 10–20 s^{-1}, processing maps showed areas of flow instability in the temperature ranges around 1000 °C and 1250 °C. Therefore, during shaping under these conditions, the location of the processing window was determined by the location of these zones and the distribution of the η parameter. Favorable values of the η parameter for particular strain rates were obtained in the area described as processing window 1, marked in blue. The boundary of this window extends from the point corresponding to the temperature of 1025 °C and the maximum strain rate, according to the isoline with the value of the parameter $\eta = 24\%$. The value of strain rate of 0.8 s^{-1} was taken as the lower limit for it. On the other hand, for higher temperatures, a line running from the point corresponding to values of strain rate of 20 s^{-1} i and temperature above 1025 °C to the

point corresponding to strain rate of 0.8 s^{-1} and temperature of 1225 °C was taken as the limit. This course of the boundary of the processing window 1 was due to the need to bypass the area of instability found in the processing map for the value of true strain 1.1 (Fig. 3e). As a result, a processing window 1 was obtained for which the values of the parameter η range from 24 to 44%. The temperature range for this window is from 1025 to 1225 °C and the range of deformation velocity is from about 6.3–20 s^{-1}. For this window, the range of values of deformation activation energy, determined from the Q-distribution map (Fig. 5b), is between 400 and 420 kJ/mol.

The processing window 2 corresponds to lower strain rates. This window is marked in orange. The upper limit of this window is the strain rate of about 6.3 s^{-1} and the lower strain rate is about 0.3 s^{-1}. On the lower temperature side, the window boundary runs according to the isoline with a parameter value of $\eta = 24\%$, and then according to the boundary of the instability region. On the higher temperature side, the window is bounded by the instability area and then by the maximum temperature 1250 °C. For this window, the values of the parameter η range from 24 to 40%, the temperature range is from 1100 to 1250 °C and the strain rate is about 0.3–6.3 s^{-1}. The value of energy of activation of high-temperature deformation Q inside window 2 ranges from 400 to 639 kj/mol, which is much wider than that of window 1.

For the remaining areas with relatively high values of the η parameter, analysis of processing maps for intermediate strain values (Fig. 3a–e) led to the exclusion of the occurrence of processing windows in these zones. It was found that as deformation increases, these zones enter the ranges of areas with negative values of the parameter ξ, leading to the risk of microstructural defects. This approach is consistent with the principles of determining processing windows based on the adopted Prasad approach.

3.5 Microstructure of samples after deformation on WUMSI simulator

The microstructures of the samples after deformation on the WUMSI simulator and after rapid cooling are summarized in Fig. 6.

Observations were made primarily to confirm or exclude the presence of microstructural defects. Microcracks occurring at grain boundaries, formed as a result of rapid cooling immediately after the test was completed, were not taken into account. Attention was paid to microstructural defects formed as a result of hot deformation. Such defects, in particular strain localization, were found for samples after deformation at 900 °C and at strain rates in the range of 0.1 to 1 s^{-1}. For these combinations of temperature and strain rate, the occurrence of

Table 2 Calculated material constants and deformation activation energy for 80MnSi8-6 steel

ε	n_1	β	α	n	Q, kJ/mol
0.05	7.161025	0.075725	0.01057	5.04825	358.472
0.2	7.072225	0.064525	0.00912	4.95770	370.521
0.5	7.246075	0.062200	0.00858	5.07255	352.893
0.8	7.368875	0.065525	0.00889	5.13273	350.561
1.1	8.542975	0.082300	0.00963	5.94650	394.978
1.2	8.843075	0.085275	0.00964	6.17495	434.614

microstructural instability, demonstrated by DMM analysis, was confirmed. For specimens after deformation at the highest temperature 1250 °C and at relatively high strain rates of 10 and 20 s^{-1}, uneven growth of primary austenite grains was found. This parameter range was also indicated as potentially leading to defects because it is located inside the region of negative value of parameter ξ. Observations of the microstructure of specimens deformed using combinations of temperature and strain rate other than those mentioned did not reveal the presence of defects associated with the hot deformation process on the WUMSI simulator.

3.6 The compression tests on a hydraulic press

The compression tests on the hydraulic press were carried out in such a way that the parameters of these tests were located on the processing maps developed by the DMM method inside the processing window, in the neutral area and inside the area of potential microstructural instability, respectively. For this reason, the following combinations of temperature and linear velocity of the upper tool were used: 1000 °C/5 mm·s^{-1} (neutral area), 1100 °C/5 mm·s^{-1} (instability area) and 1200 °C /20 mm·s^{-1} (processing window 2). The microstructure of 80MnSi8-6 steel was evaluated after deformation and cooling in air. Figure 7 summarizes, respectively, a photo of the press work zone with the heated sample (Fig. 7a), the approximate locations of the test parameters on the processing maps (Fig. 7b), the microstructure of the starting material (Fig. 7c) and the microstructure in the deformed state under the adopted conditions (Fig. 7d–f).

The microstructure seen in Fig. 7 the microstructure consists of bainite and martensite and contains some residual austenite. In the case of the sample after compression deformation at 1000 °C and linear tool speed of 5 mm·s^{-1}, the microstructure is more fragmented than that obtained by the other compression variants. The reason may be that at lower strain temperature the DRV and DRX processes occur less efficiently. It can be assumed that the occurrence of austenite with higher dislocation density will
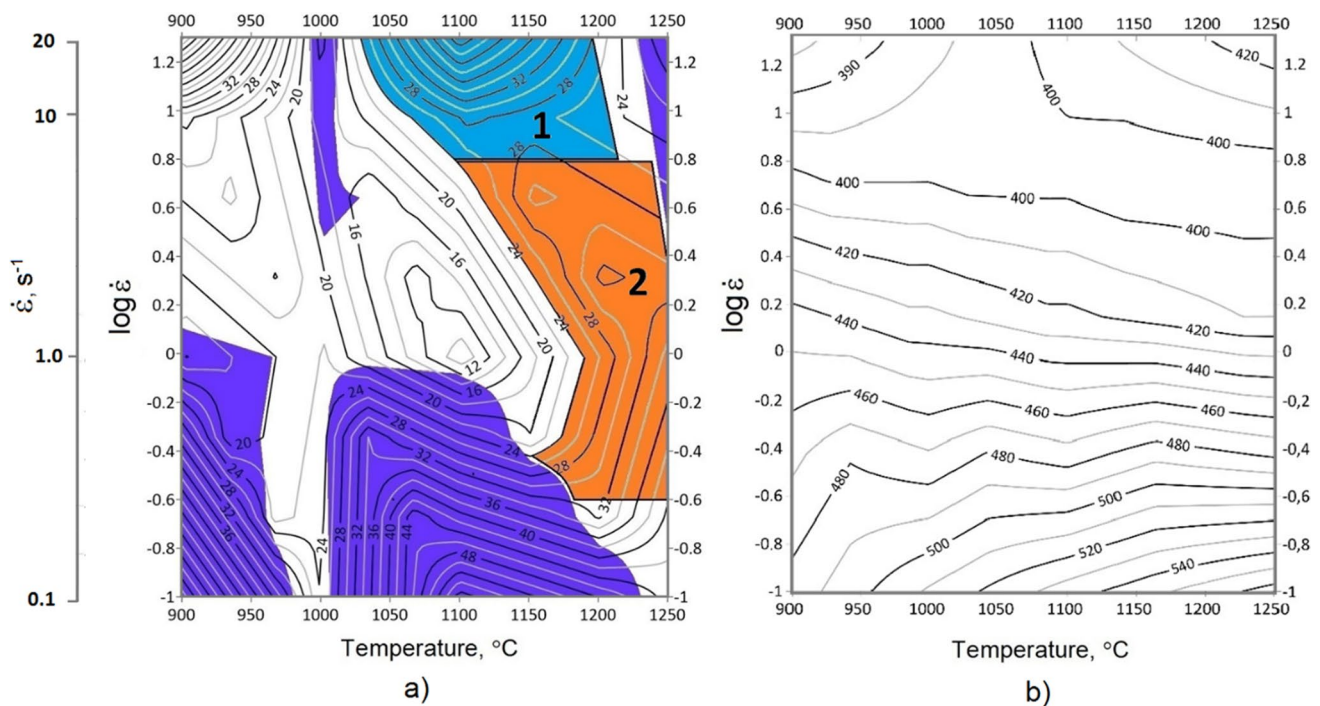

Fig. 5 Developed for 80MnSi8-6 steel and for the final true strain value 1.2: **a** processing map with processing windows applied, **b**—distribution map of activation energy of deformation Q
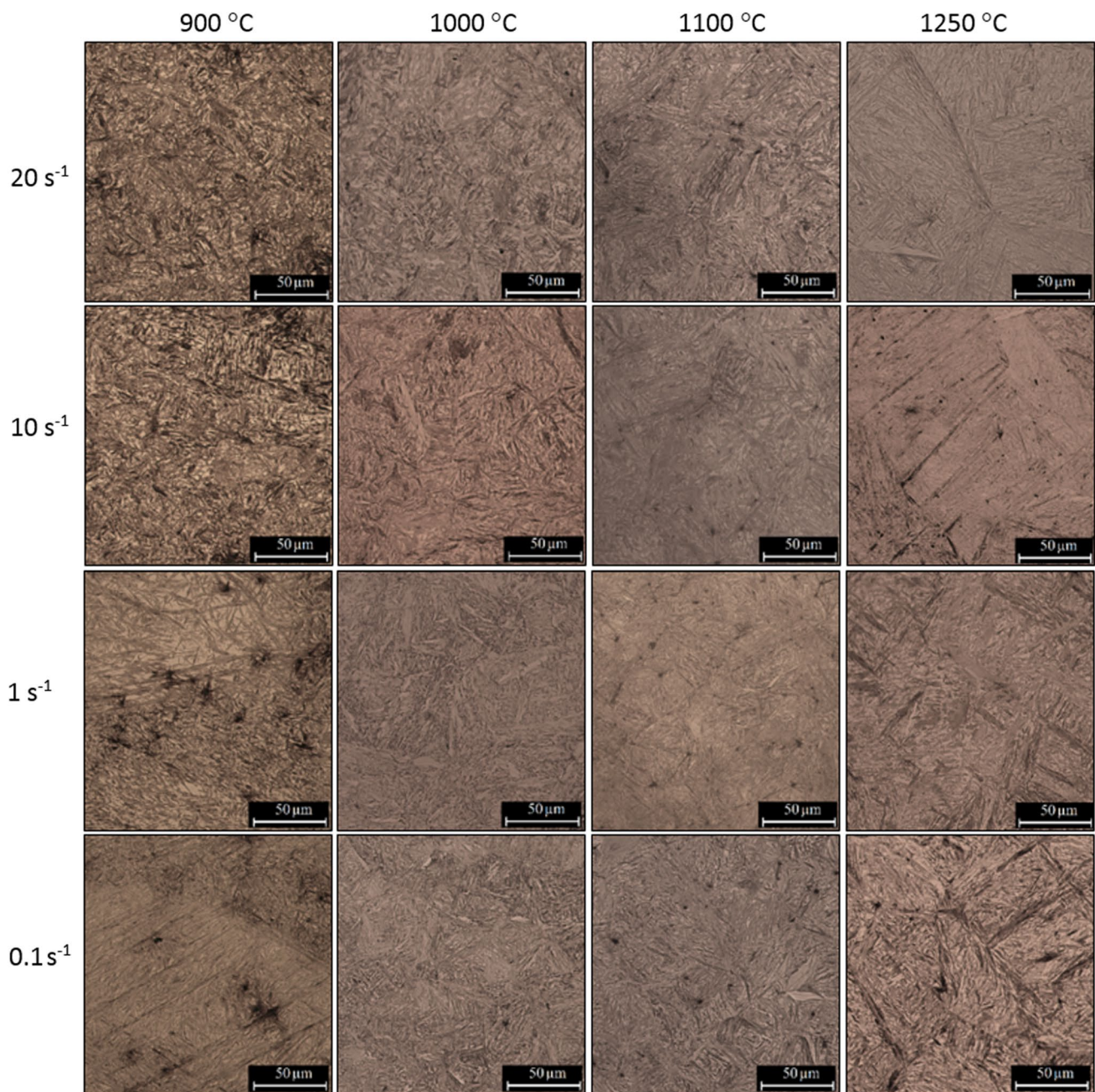
Fig. 6 Effect of test parameters on the microstructure of specimens after deformation on the WUMSI simulator and after their rapid cooling. The specimens in cross-section passing through the axis of symmetry, images in the center of the specimen. Etched

significantly affect the kinetics of phase transformations. The microstructure of the sample deformed at 1200 °C is characterized by a higher proportion of martensite, which may be due to a higher heat transfer rate in the first cooling stage. Local inhomogeneities in the microstructure were found in samples heated to 1100 °C and then compressed with linear tool speed of 5 mm·s^{-1}, which, in the processing map (Fig. 7b), corresponds to the location inside the area of potential microstructural instability. Directional bands were found, which could indicate the location of the deformation (Fig. 7f), as can be seen at lower magnifications. However, a homogeneous and defect-free microstructure prevailed on the observed cross-section. For the remaining samples, after compression using parameters corresponding to the interior of processing window 1 and the neutral zone, no microstructure defects were found.
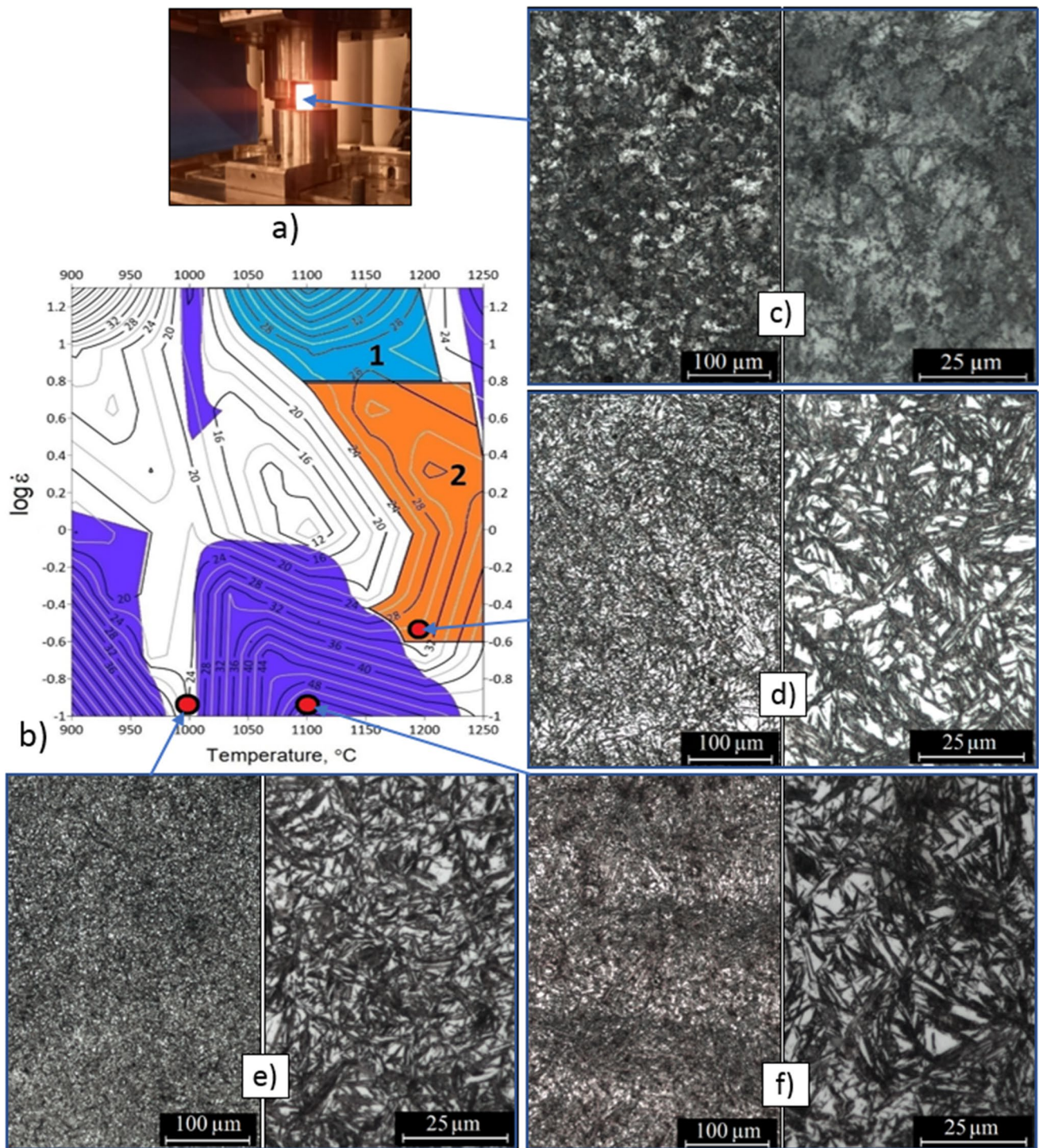
Fig. 7 The compression tests on the hydraulic press: **a**—working zone of the press, **b**—diagram of the location of the test parameters on the processing maps, **c**—microstructure of the starting material and **d–e** microstructures after deformation: **d** – temperaturę 1200 °C and linear tool speed of 20 mm·s^{-1}, **e**—temperature 1000 °C and linear tool speed of 5 mm·s^{-1}, **f**—temperature 1100 °C and linear tool speed of 5 mm·s^{-1}
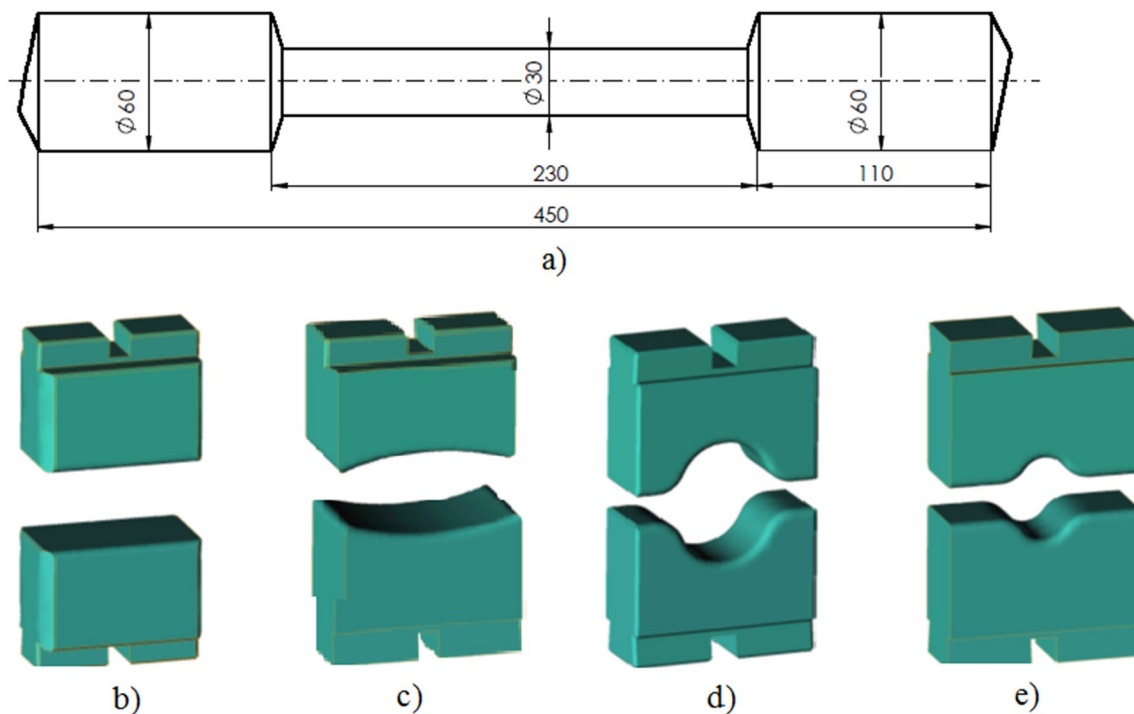
Fig. 8 Schematics: **a**—of the forging and **b–e**—of the designed tools

This applied to parts of the center of the forgings, as well as zones near its lateral edges.

3.7 Integrated FEM and DMM analysis of a selected multi-stage hot forging process

For numerical FEM analysis taking into account the modeling of changes in parameter values obtained by the DMM method, the process of multi-stage hot free forging of a sample which shape and dimensions are shown in Fig. 8a. The forging process was modeled on a hydraulic press with a pressing force of 5000 kN and a constant speed of movement of the upper tool. A cylinder with a diameter of 85 mm and a length of 140 mm was adopted as the feedstock for forging. On one face of the feedstock, a holder for a manipulator with a diameter of 40 mm and a length of 50 mm was designed. The chosen shape allowed for a forging degree of 2 in the outer segments and a varying amount of deformation in the forging volume.

Since the speed used during free forging on hydraulic presses is low, therefore, a constant upper tool movement speed of 10 mm·s^{-1} was adopted for the simulation. Taking into account the initial feedstock diameter of 85 mm, the dimensions of the forging during subsequent forging stages and the final dimensions of the forging, the strain rate during the process corresponded to the lowest range in the processing maps, staying within this range.

In the first stage, a series of preliminary FEA simulations were performed in QForm software, using various variations that included temperature, tool shape (Fig. 8b–e), feed and rotation values, and others. In this way, a multi-stage forging procedure was developed, which made it possible to obtain a forging with the correct shape and without surface defects. The upper limit forging temperature 1250 °C was adopted, and the moments of inter-process reheating were determined. In the variant of multi-stage forging selected as favorable, the operations of elongating the feedstock into a square cross-section and then into an octagonal profile were applied successively. Rounding was carried out in shaping tools. Then, the forging of the inner part was modeled with spherical and shaped tools. To carry out the established operations, four sets of tools were developed, the shapes of which are shown schematically in Fig. 8b–e. Preliminary operations were performed in flat tools (Fig. 8b). Then, in order to remove the defects found during FEM modeling on the surface of the forging, tools with spherical faces were used (Fig. 8c). Rounding to final diameters was done by forging the feedstock to a diameter of 60 mm using the tools in Fig. 8d and forging the middle part of the feedstock to a diameter of 30 mm using the set of tools in Fig. 8e.

Then, an integrated FEM/DMM numerical analysis was designed and performed for the pre-developed FEM of the multi-stage forging procedure. Data from the DMM analysis were introduced into the QForm software using previously developed subroutines that included the results of the DMM analysis. In this way, the distributions of instability parameter (ξ parameter), strain rate sensitivity
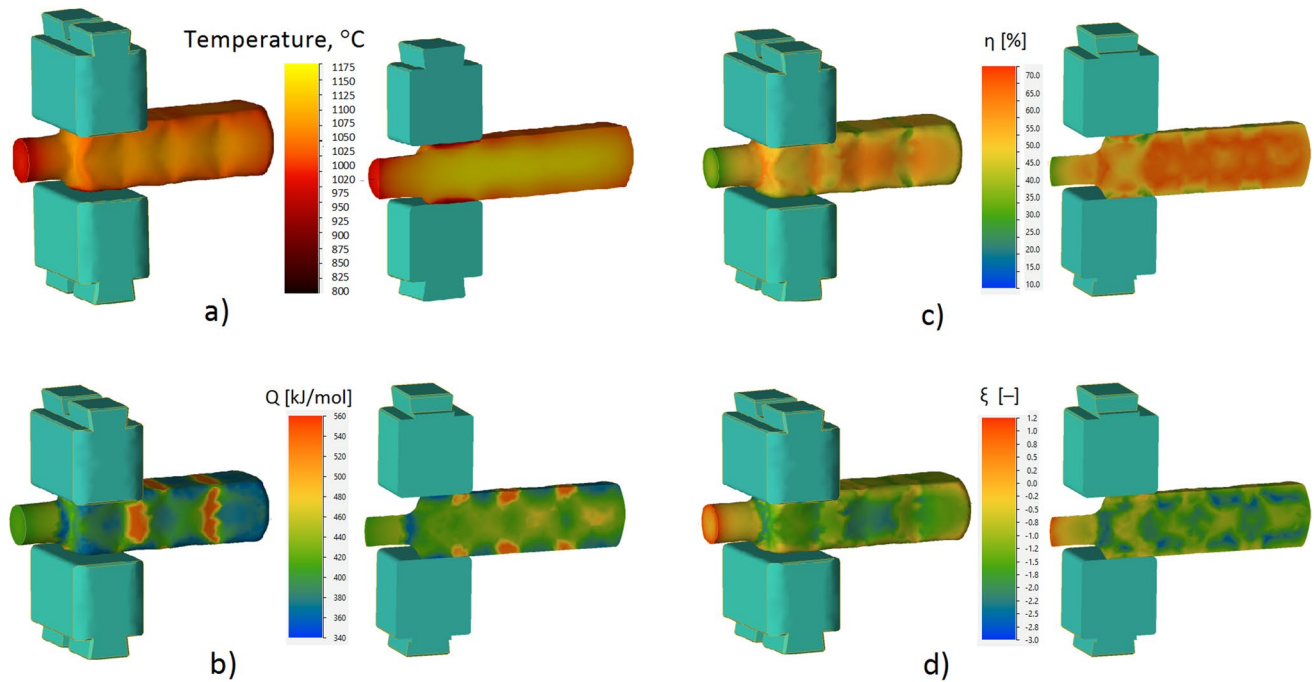
Fig. 9 Results of the integrated FEM/DMM analysis of the multi-stage forging process of 80MnSi8-6 steel. The forging stage into a square shape between flat tools. Presented on the surface and in the center of the forging volume distributions of: **a** – temperature, **b**—hot deformation activation energy Q, **c**—strain rate sensitivity parameter (η parameter) and **d**—instability parameter (ξ parameter)

parameter (η parameter) and hot deformation activation energy Q were included in the FEM calculations, depending on the values of strain, strain rate and temperature. Example results of modeling of the hot forging process of a multi-stage forging of 80MnSi8-6 steel with DMM analysis are summarized in Figs. 9, 10, 11. Figure 9 shows the results of modeling of the feedstock elongation stage into a square shape between flat tools. The temperature distributions on the surface and inside the volume of the forged semi-finished product (Fig. 9a), and the corresponding distributions of Q, η and ξ (Fig. 9b–d) are summarized. Under the conditions corresponding to the deformation set at this stage and the temperature determined in Fig. 3a, high values of η are observed, reaching about 65%. These correspond to the values of the η parameter in the processing maps developed for true strain of about 0.5, for the lowest values of strain rate and for the temperature value corresponding to the distribution in the figure (Fig. 3c). The values of Q vary in the direct strain zone in the range from 340 to 560 kJ/mol. The parameter ξ takes mainly negative values, which is due to the realization of deformation inside the region of potential microstructural instability. Due to the same values of relative feed in successive deformations, the distributions of DMM values (Fig. 9b–d) have an approximately repeatable shape. Slight differences are due to the decrease in material temperature during the realization of successive deformations and during the time

between them, when the position of the forged feedstock is changed between tools.

Figure 10 summarizes the results of integrated modeling of the final forging operation, which consists of elongating the inner part of the feedstock to a diameter of 30 mm between shaping tools. Figure 10a–c shows the distributions of the parameters in which the deformation was carried out in the forging volume, and Fig. 10 d–f shows the distributions of the parameters η and ξ and the distribution of Q values. In order to further analyze the distributions of the individual parameters in the direct deformation zone, their values were compiled and compared at points lying in the center of the deformed section (point A), in the zone near the contact surface with the upper anvil (B) and in the lateral zones (C and D), respectively. The distributions of the individual parameters in the deformation zone are shown in Fig. 11a–f. Also included are the results of measuring the values of these parameters at points A–D (Fig. 11h). Significant differences were observed in the values of η and ξ and Q depending on where they were measured in the direct deformation zone. Factors such as the cooling of the material due to contact with the cooler top tool (Fig. 11b) or the low value of the strain rate resulting from the frictional force on the contact surface with the upper tool (Fig. 11a) lead to variations in the values of the parameters obtained by the DMM method (Fig. 11d–e) and the
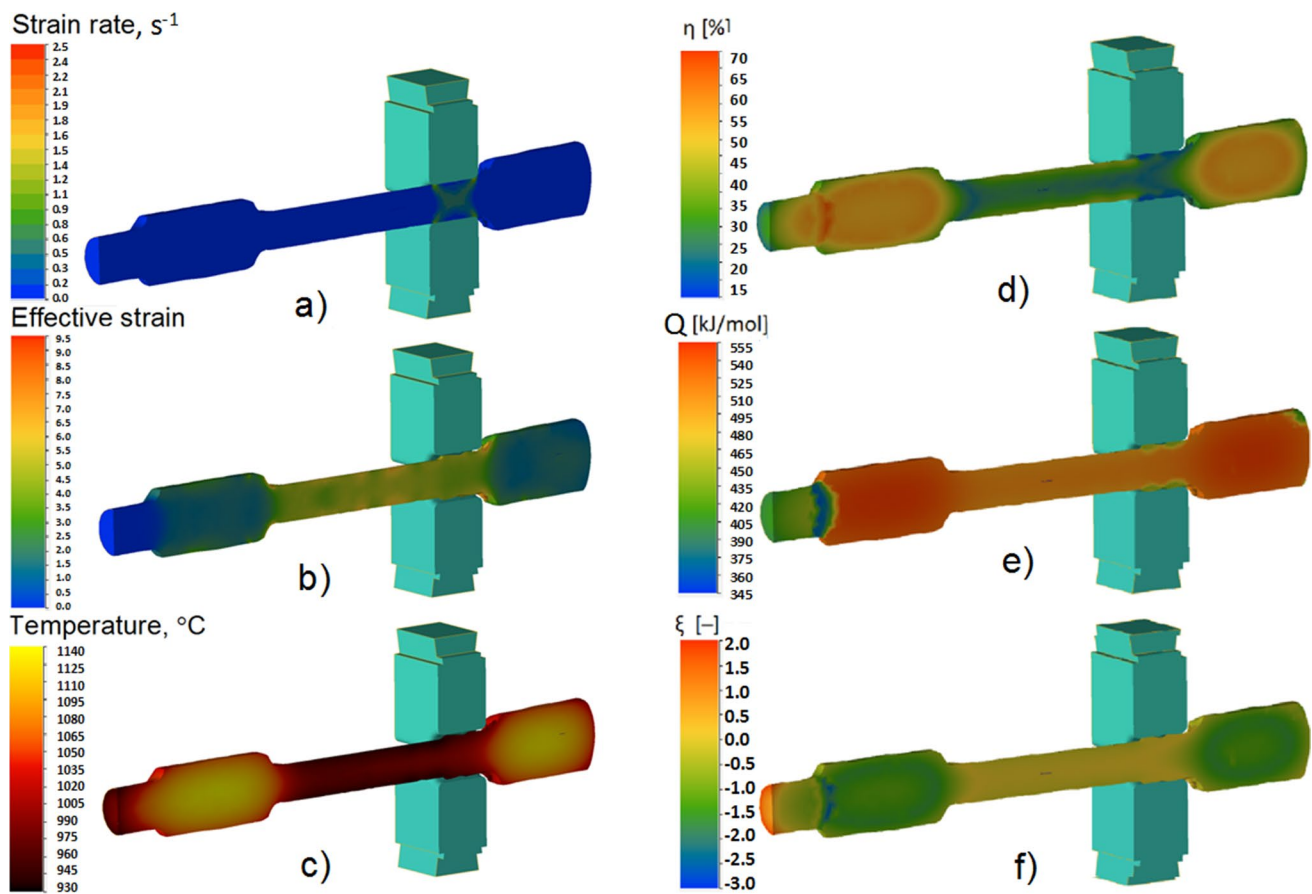
Fig. 10 Results of integrated FEM/DMM analysis for an example stage of the multi-stage forging process of 80MnSi8-6 steel. The final operation of elongation of the inner part with a diameter of 30 mm between shaping tools. The distributions obtained in the center of the forging volume: **a** – strain rate, **b** – effective strain, **c** – temperature, and the corresponding distributions of: **d**—hot deformation activation energy Q, **e**—strain rate sensitivity parameter (η parameter) and **f**—instability parameter (ξ parameter)

value of hot deformation activation energy Q (Fig. 11f) in the deformation zone. Interpretation of these relationships can facilitate decisions on process modifications, such as changing the deformation strategy or inter-heating process. By influencing the local distributions of temperature, strain values and strain rates (Fig. 11a–c) in this way, the corresponding distributions of η, ξ and Q (Fig. 11d–f) can be changed to more favorable ones. This is especially true for those free forging operations that produce defects, such as laps. Therefore, the juxtaposition of the process parameter distributions and the corresponding η, ξ and Q parameter distributions (Figs. 9, 10, 11) in the volume of the shaped forging or in the single deformation zone allows the effective use of DMM results and energy analysis, which is difficult in the case of multi-stage forging processes on the basis of the commonly used processing maps or maps of Q value distributions in the processing space.

4 Discussion

Using the results of plastometer tests on the WUMSI simulator, flow curves were developed to describe the response of 80MnSi8-6 steel to changes in deformation conditions and are the basis for DMM analysis and integrated FEM/DMM modeling. The general nature of the flow curves is typical for steel. For particular combinations of temperature and strain rate, stages of rapid increase in flow stress due to strain hardening were identified, as well as values of true strain necessary to reach peak stress (σ_p). As deformation progressed, the steel showed a decrease in stress values, which is due to the removal of the effects of strengthening by the heat-activated dynamic healing phenomena; dynamic recovery (DRV) and dynamic recrystallisation (DRX). As the true strain values increase, the effects of work hardening and deformation softening reach
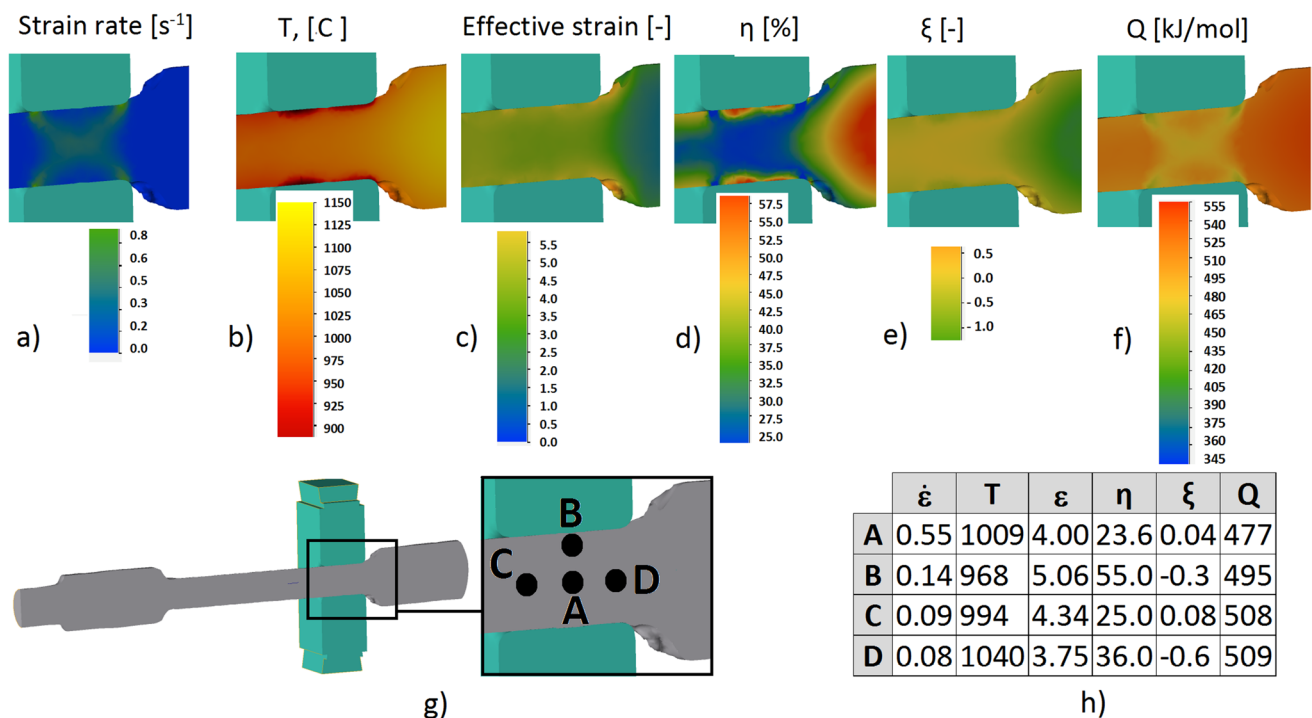
	$\dot{\varepsilon}$	T	ε	η	ξ	Q
A	0.55	1009	4.00	23.6	0.04	477
B	0.14	968	5.06	55.0	-0.3	495
C	0.09	994	4.34	25.0	0.08	508
D	0.08	1040	3.75	36.0	-0.6	509

Fig. 11 Results of integrated FEM/DMM analysis of 80MnSi8-6 steel in the region of the deformation zone. Selected step during elongation operation between shaping tools. **a–e**—distributions of values in the deformation zone, **g**—diagram showing the analysis points in the deformation zone, and **h**—summary of parameter values in points A–D

an equilibrium state. There was no change in the sensitivity of the test material to a change in test temperature, for all strain rates used, increasing the temperature resulted in a proportional decrease in true strain values. It was also noted that as the test temperature changed, the nature of the curves changed regularly. Increasing the strain rate led to an increasing value of the stress in the initial stages of deformation and a greater decrease in its value in the advanced stage of deformation.

It was shown that the deformation activation energy Q in the case of 80MnSi8-6 steel varies over a fairly wide range as the value of true strain increases (Fig. 4 and Table 2) and depends on the temperature and strain rate. Besides the differences in Q values, the nature of changes in this value in the process space is also important. When using equipment operating in a narrow range of speeds, such as hydraulic presses, it is advantageous when Q values do not change significantly in this range as a result of temperature changes. For relatively low strains, up to 0.2, isoline courses strongly sloped from the horizontal direction are observed, indicating changes in Q values during material cooling as the process proceeds. Significant changes in Q values following a decrease in temperature during successive deformations can cause flow instability and lead to the formation of microstructural defects, such as strain localization. This is especially true for those areas in the Q distribution

maps where the isolines are concentrated, which is the decrease or increase in Q value due to temperature changes occurs rapidly. For deformations in the range of 0.5 and higher, the trends of the isolines on the Q distribution maps change. A significant part of the isolines show a horizontal or near horizontal course. This means that the plastic flow of the material during successive operations of the multistage forging process with a constant or similar strain rate requires the expenditure of a similar value of deformation activation energy Q, regardless of the feedstock temperature. Such a condition is favorable and can be assumed to lead to uniform and stable microstructural changes. In the case of 80MnSi8-6 steel for strain rates above 0.2, a favorable region is observed in the strain rate range from 1 to 4 s^{-1}. However, it should also be noted that in the low strain rate region where multi-stage forging was modeled, the distance between successive isolines is large, indicating that the value of Q does not change significantly as a result of temperature decrease during forging.

The average value of deformation activation energy (Table 2) is within the range typical of steels. For example, a compilation of Q values for a selection of four different TRIP-type steels compiled by Reyes-Calderon et al. [49] for a true strain value of 0.8 contained results ranging from 366 to 425 kJ/mol. In contrast, Cabanas et al. [50] for the same value of true strain of Fe–Mn steel obtained Q = 279 kJ/mol.

The average Q value determined in this paper for a strain of 0.8 (Table 2) was 351 kJ/mol. On the other hand, Zhao et al. [51] determined Q values for low-carbon steel at true strain values around 1.0, obtaining values ranging from 305 kJ/mol for low strain rates to 475 kJ/mol and for high strain rates. The authors of the present study for a similar strain value of 1.1 and for the full range of strain rates obtained a value of Q of 394 kJ/mol.

Observations of the microstructure of the specimens after deformation on the WUMSI simulator and after their rapid cooling (Fig. 6) were aimed at demonstrating or excluding the presence of defects formed during the hot deformation process in the adopted sets of test parameters. Defects, in particular, strain localization, were found for the samples in the deformed state at the lowest temperature 900 °C and at strain rates in the range of 0.1–1 s^{-1}. For these combinations of temperature and strain rate, the presence of microstructural instability, as identified by DMM analysis, was confirmed. Thus, it should be assumed that during forging in the low strain rate range, the temperature should not be allowed to drop to this value. In the case of specimens after deformation at the highest temperature 1250 °C and at relatively high strain rates of 10 and 20 s^{-1}, uneven growth of primary austenite grains was observed. This parameter range was also pointed out as potentially leading to the formation of defects, since it is located inside the region of negative value of parameter ξ. This confirmed the correctness of the position of processing window 1, which was reduced by this area. Observations of the microstructure of specimens deformed using combinations of temperature and strain rate other than those mentioned did not reveal defects associated with the hot deformation process on the WUMSI simulator.

The compression tests on a 5000 kN hydraulic press were carried out in the low strain rate range, below 0.5 s^{-1}. According to the authors, validation of the processing maps in this area was necessary because the conditions of the integrated FEM/DMM analysis of the multi-stage forging process on a hydraulic press corresponded to this area in the process space. The samples were cooled in air after deformation. This modeled process conditions similar to those found on an industrial line in a forge plant. Therefore, observations of the microstructure allowed not only inspection conducted for defects, but also qualitative assessment of the microstructure that is formed during deformation and subsequent cooling at natural speed. This is important because knowledge about the evolution of the microstructure resulting from changes in deformation parameters allows for a better understanding of the impact of process parameters on product properties, as demonstrated, among others, in [52]. For specimens compressed using parameters corresponding to the interior of processing window 1 and the neutral zone, no microstructural defects were found. Observations of the specimen deformed under conditions corresponding to the location of the zone with negative instability parameter values revealed the occurrence of bands of directional flow, indicating the localization of the deformation. However, the places where such effects occurred were few, and the observed cross-section was dominated by a microstructure that was homogeneous and free of defects. It should be assumed that areas with negative values of the ξ parameter indicate for the 80MnSi8-6 steel under study those combinations of temperature and strain rate where the risk of microstructural instability is increased, but in practice, it does not have to occur.

Preliminary FEM numerical analysis of the hot multi-stage forging process on a hydraulic press allowed the development of tool sets that enabled the manufacture of a forging of the assumed shape. The modeling of different forging variants also made it possible to develop such a sequence of operations that led to the production of a defect-free product of the assumed geometry with the assumed degree of forging 2. During the calculations, the current capabilities of the QForm software were used, including the options for FEM modeling of processes performed in multiple sequences, tool replacement, inter-operational rotation and displacement of the feedstock, inter-operational reheating and other advanced functions. During the FEM analysis, it was assumed that the forging process would be carried out on a 5000 kN hydraulic press. Since the speed used during free forging on hydraulic presses is low, therefore, a constant upper tool movement speed of 10 mm·s^{-1}. Taking into account the initial feedstock diameter of 85 mm, the dimensions of the forging during the subsequent forging stages and the final dimensions of the forging, the strain rate during the process corresponded to the lowest range in the process space, staying within this range. The resulting data provided a starting point for performing an integrated FEM / DMM analysis.

The data obtained from the DMM analysis were implemented into the QForm software using subroutines, developed in the LUA programming language. The results of this analysis confirmed that the range of low strain rates in the processing maps developed for 80MnSi8-6 steel (Figs. 3 and 5) is difficult to interpret. On one hand, this is the area where the DMM analysis showed the presence of areas of potential microstructural instability, both for the final strain rate of 1.2 and at intermediate stages (Fig. 3), especially in the true strain range of 0.2–0.8. On the other hand, the strain rate sensitivity parameter values show the highest values in this area, especially in the temperature ranges of 1025–1200 °C and below 950 °C. By definition, in these areas, the plastic formability of the material and the ability to remodel the microstructure are high. For the analyzed steel in the lower area of the processing maps, it can be seen that zones with high values of the η parameter coincide with areas of defect risk. Shaping in successive stages of individual segments of the product leads to a significant variation of temperature

and the amount of strain in the volume of the forging. The observed differences between segments, particularly those shaped in separate operations, lead to non-uniform distributions of the η parameter and the presence of negative values of the ξ parameter in many areas. Therefore, variations in microstructure within individual segments are expected. In this case, the role of processing maps is to correlate the non-uniform deformation with potential non-uniformity in the microstructure. Hence, combining the DMM method with FEM is seen as a beneficial solution by the authors. An example of adopting such an approach is the work by Łukaszek-Sołek [40]. By expanding the basic options of the software based on the FEM with subroutines that allow for determining numerical distributions of strain rate sensitivity parameters, effective power dissipation, and flow instability in a specific forging, it is possible, among other things, to identify critical areas within the forging volume that require special attention, such as microstructure control or non-destructive testing. Such analysis can be conducted both throughout the entire volume of the forging at a given stage of its shaping (Figs. 9, 10), as well as in the deformation zone when applying a single blow between the tools (Fig. 11). Standard phenomena occurring during deformation, such as uneven deformation or temperature drop due to heat transfer to cooler tools, can be quantitatively analyzed. Additionally, distributions of parameters obtained from DMM analysis can also be examined. The outcomes of such analysis could include decisions about performing (or omitting) inter-stage heating at a certain forging stage, modifications to the forging sequence, or changes in temperature range. Each of these modifications leads to changes in the processing space of subsequent deformation parameters, which allows for more favorable adjustments to DMM parameters. These changes become evident during post-processing and analysis of FEM modeling results. On the other hand, FEM/DMM analysis in the zone of individual deformations (Fig. 11) can be applied when local material quality issues arise at any forging stage, such as challenging-to-eliminate defects. In such cases, expanding the FEM results with a local analysis of distributions of instability parameter, strain rate sensitivity parameter, and hot deformation activation energy Q can be helpful in avoiding such defects.

The mentioned benefits arising from expanding the scope of FEM calculations with distributions of DMM parameters and Q provide a basis for stating that such an approach significantly enhances the capabilities of typical numerical analysis of hot forging processes and enables a more comprehensive interpretation of modeling results. The outcomes can lead to improved manufacturing process efficiency and higher forging quality. This is particularly relevant for products with varying dimensions, manufactured from advanced materials, as evidenced by other studies, including references [35, 36, 40]. The obtained results demonstrate that nanobain steels, including the investigated 80MnSi8-6 steel, fit well into this category of materials.

5 Conclusions

The results of the deformation behavior investigations of 80MnSi8-6 steel, verified through tests and evaluation of the microstructure of samples after deformation, as well as the outcomes of the integrated FEM / DMM modeling of the multi-stage forging process, led to the following conclusions:

1. The flow curves of 80MnSi8-6 steel, developed based on data from plastometric tests, allowed for the identification of phenomena occurring during hot deformation of this material and the assessment of the influence of deformation parameters on their course. These flow curves were used as a basis for conducting the extended DMM analysis, incorporating distributions of hot deformation activation energy Q values.
2. The development of processing maps and the analysis of Q value variations enabled the identification of process windows and potentially unfavorable combinations of deformation parameters within the investigated range for the studied steel. The processing maps, especially in regions of instability, were verified by microstructure observations.
3. Hot compression tests conducted on a hydraulic press allowed for the validation of the accuracy of DMM results at low strain rates and the evaluation of the state of the microstructure formed during deformation and cooling under conditions similar to those in industrial lines.
4. The implementation of DMM analysis results into the FEM software enables modeling within a broader range than standard. The overall and local assessment of distributions of parameters η, ξ, and Q in the deformation zone during successive operations provides a more accurate evaluation of material deformability and the prediction of the occurrence of microstructural defects. The obtained data, when properly interpreted, facilitate process efficiency improvement, such as through modifications to forging sequences or changes in reheating strategies.
5. The results of FEM modeling extended with the results of DMM analysis and distributions of hot deformation activation energy can serve as a valuable tool in designing hot deformation processes for 80MnSi8-6 steel. This is particularly relevant for lengthy processes involving multiple operations, such as multi-stage free forging on presses with low strain rates.

Data availability The data that support the findings of this study are available from the corresponding author upon reasonable request.

Declarations

Conflict of interest The authors have no conflicts of interest to declare that are relevant to the content of this article.

Ethical approval This article does not contain any studies with human participants or animals performed by any of the authors.

References

1. Bhadeshia HKDH. Atomic mechanism of the bainite transformation. J Heat Treatm Mat. 2017;72(6):340–5.
2. Zhang FC, Wang TS, Zhang P, Zhang CL, Lv B, Zhang M, Zhang YZ. A novel method for the development of a low-temperature bainitic microstructure in the surface layer of low-carbon steel. Scr Mater. 2008;59:294–6.
3. Królicka A, Żak A, Kuziak R, Radwański K, Ambroziak A. Decomposition mechanisms of continuously cooled bainitic rail in the critical heat-affected zone of a flash-butt welded joints. Mater Sci-Pol. 2021;39(4):615–25. https://doi.org/10.2478/msp-2022-0002.
4. Avishan B, Talebi P, Tekeli S, Yazdani S. Producing nanobainite on carburized surface of a low-carbon low-alloy steel. JMEPEG. 2023;32:211–20.
5. Zhu Z, Han J, Li H, Lu C. High temperature processed high Nb X80 steel with excellent heat-affected zone toughness. Mater Lett. 2016;163:171–4.
6. Garcia-Mateo C, Caballero FG, Sourmail T, Smanio V, de Andres CG. Industrialised nanocrystalline bainitic steels. Design approach. Int J Mater Res. 2014;105(8):725–34.
7. Królicka A, Janik A, Żak A, Radwański K. The qualitative–quantitative approach to microstructural characterization of nanostructured bainitic steels using electron microscopy methods. Mater Sci Pol. 2021;39(2):188–99. https://doi.org/10.2478/msp-2021-0017.
8. Sourmail T, Garcia-Mateo C, Caballero FG, Morales-Rivas L, Rementeria R, Kuntz M. Tensile ductility of nanostructured bainitic steels: influence of retained austenite stability. Metals. 2017;7:31–7.
9. Caballero FG, Bhadeshia HKDH, Mawella KJA, Jones DG, Brown P. Design of novel high strength bainitic steels: Part 2. Mater Sci Technol. 2001;17:517–22.
10. Sourmail T, Caballero FG, Garcia-Mateo C, Smanio V, Ziegler C, Kuntz M, Elvira R, Leiro A, Vuorinen E, Teeri T. Evaluation of potential of high Si high C steel nanostructured bainite for wear and fatigue applications. Mater Sci Technol. 2013;29(10):1166–73.
11. Rios-Diez O, Aristizabal-Sierra R, Serna-Giraldo C, Eres-Castellanos A, Garcia-Mateo C. Wear behavior of nanostructured carboaustempered cast steels under rolling-sliding conditions. J Mater Res Technol. 2021;11:1343–55.
12. Du Y, Wang X, Zhang D, Wang X, Ju C, Jiang B. A superior strength and sliding wear resistance combination of ductile iron with nanobainitic matrix. J Mater Res Technol. 2021;11:1175–83.
13. Mishra B, Sukumar G, Senthil PP, Reddy PRS, Singh BB, Ramakrishna B, Kumar KS, Madhu V. Ballistic efficacy of carbide free high strength nano-structured bainitic armour steels. Def Sci J. 2023;73(2):131–9.
14. Kowalczyk K, Jabłońska M, Rusz S, Junak G. Influence of recrystallization annealing on the properties and structure of low-carbon ferritic steel IF. Arch Metall Mater. 2018;63(4):1957–61. https://doi.org/10.24425/amm.2018.125130.
15. Sourmai T. Bainite and superbainite in long products and forged applications. HTM. 2017;72(6):371–8.
16. Garcia-Mateo C, Caballero FG, Sourmail T, Cornide J, Smanio V, Elvira R. Composition design of nanocrystalline bainitic steels by diffusionless solid reaction. Met Mater Int. 2014;20(3):405–15.
17. Jabłońska MB, Śmiglewicz A, Niewielski G. The effect of strain rate on the mechanical properties and microstructyre of the high-Mn steel after dynamic deformation tests. Arch Metall Mater. 2015;60(2):577–80. https://doi.org/10.1515/amm-2015-017.
18. Caballero FG, Bhadeshia HKDH, Mawella KJA, Jones DG, Brown P. Very strong low temperature bainite. Mater Sci Technol. 2002;18:279–84.
19. Garcia-Mateo C, Caballero FG. Design of carbide-free low-temperature ultra high strength bainitic steels. Int J Mat Res. 2007;98(2):137–43.
20. Leiro A, Vuorinen E, Sundin K-G, et al. Wear of nano-structured carbide-free bainitic steels under dry rolling-sliding conditions. Wear. 2013;298–299:42–7.
21. Prasad YVRK, Gegel HL, Doraivelu SM, Malas JC, Morgan JT, Lark KA, Barker DR. Modeling of dynamic material behavior in hot deformation: forging of Ti-6242. Metall Mater Trans A. 1984;15:1883–9.
22. Prasad YVRK, Sasidhara S, editors. Hot working guide: a compendium of processing maps. Materials Park: ASM International; 1977. p. 108–10.
23. Raj R. Development of a processing map for use in warm-forming and hot-forming processes. Metall Trans A. 1981;12:1089–97.
24. Babu KA, Mandal S, Athreya C, Shakthipriya B, Sarma VS. Hot deformation characteristics and processing map of a phosphorous modified super austenitic stainless steel. Mater Des. 2017;115:262–75.
25. Li H, Wang H, Liang X, Liu H, Liu Y, Zhang X. Hot deformation and processing map of 2519a aluminum alloy. Mater Sci Eng A. 2011;528:1548–52.
26. Krawczyk J, Łukaszek-Sołek A, Śleboda T, Bała P, Bednarek S, Wojtaszek M. Strain inducted recrystallization in hot forged Inconel 718 alloy. Arch Metall Mater. 2012;57(2):593–603. https://doi.org/10.2478/v10172-012-0063-y.
27. Jablonska MB, Kowalczyk K. Microstructural aspects of energy absorption of high manganese steels. Procedia Manuf. 2019;27:91–7.
28. Prasad YVRK, Seshacharyulu T. Modelling of the hot deformation for microstructural control. Int Mater Rev. 1998;43:243–58.
29. Chegini M, Aboutalebi MR, Seyedein SH, Ebrahimi GR, Jahazi M. Study on hot deformation behavior of AISI 414 martensitic stainless steel using 3D processing map. J Manuf Process. 2020;56:916–27.

30. Zhou PW, Song YR, Jiang HW, Wu YC, Zong YY. Hot deformation behavior and processing maps of BG801 bearing steel. J Mater Res Technol. 2022;18:3725–38.

31. Fu X, Bai P, Yang J. Hot deformation characteristics of 18Cr-5Ni-4Cu-N stainless steel using constitutive equation and processing map. Metals. 2020;10(82):1–15. https://doi.org/10.3390/met10010082.

32. Li Q, Bu H, Han J, Li M. Dynamic recrystallization behavior and processing maps of 5CrNiMoV steel during hot deformation. Mater Res Express. 2023;10: 046519. https://doi.org/10.1088/2053-1591/acce22.

33. Ye L, Zhai Y, Zhou L, Wang H, Jiang P. The hot deformation behavior and 3D processing maps of 25Cr2Ni4MoV steel for a super-large nuclear-power rotor. J Manuf Processes. 2020;59:535–44.

34. Zeng J, Wang F, Dong S, Jin L, Fan Y, Dong J. Optimization of hot backward extrusion process parameters for flat bottom cylindrical parts of Mg-8Gd-3Y alloy based on 3D processing maps. Int J Adv Manuf Technol. 2020;108:2149–64.

35. Chen X, Si Y, Bai R, Zhang X, Li Z. Hot formability study of Cr5 alloy steel by integration of FEM and 3D processing maps. Materials. 2022;15(4801):1–22. https://doi.org/10.3390/ma15144801.

36. Chen X, Du Y, Lian T, Du K, Huang T. Hot workability of ultra-supercritical rotor steel using a 3-D processing map based on the dynamic material model. Materials. 2020;13:20.

37. Hawryluk M, Rychlik M, Ziemba J, Jasiak K, Lewandowski F, Dudkiewicz Ł. Analysis of the production process of the forked forging used in the excavator drive system in order to improve the currently implemented technology by the use of numerical modeling. Mater Sci-Pol. 2021;39(2):227–39. https://doi.org/10.2478/msp-2021-0020.

38. Liu J, Cui Z, Li C. Analysis of metal workability by integration of FEM and 3-D processing maps. J Mater Process Technol. 2008;205:497–505.

39. Lin CN, Tzeng YC, Lee SL, Fuh YK, Łukaszek-Sołek A, Lin CY, Chen MC, Pan TA. Optimization of hot deformation processing parameters for as-extruded 7005 alloys through the integration of 3D processing maps and FEM numerical simulation. J Alloys Compd. 2023;948(169804):1–14.

40. Łukaszek-Sołek A. Application of dynamic material model method in drop forging process. Krakow: AGH University of Science and Technology Press; 2015.

41. Christiansen P, Martins PAF, Bay N. Friction compensation in the upsetting of cylindrical test specimens. Exp Mech. 2016;56:1271–9. https://doi.org/10.1007/s11340-016-0164-z.

42. Gomez-Marquez D, Ledesma-Orozco E, Hino R, Aguilera-Gomez E, Korpała G, Prahl U. Numerical study on the hot compression test for bulk metal forming application. SN Appl Sci. 2022. https://doi.org/10.1007/s42452-022-05093-x.

43. Łyszkowski R, Bystrzycki J. Hot deformation and processing maps of a Fe-Al intermetallic alloy. Mater Charact. 2014;96:196–205.

44. Prasad YVRK, Seshacharyulu T. Modelling of the hot deformation for microstructural control. Int Mater Rev. 1998;43:243–58.

45. Zhu Y, Cao Y, He Q, Zhang J, Luo R, Di H, Huang G, Liu Q. Three-dimensional hot processing map of a nickel-based superalloy (Alloy 925) established by modified artificial neural network model. Intermetallics. 2022;141: 107433.

46. Wang L, Liu F, Cheng JJ, Zuo Q, Chen CF. Hot deformation characteristics and processing map analysis for nickel-based corrosion resistant alloy. J Alloys Comp. 2015;623:69–78.

47. Prasad YVRK. Processing maps. J Mater Eng Perform. 2003;12(6):638–45.

48. Lin YC, Chen XM. A critical review of experimental results and constitutive descriptions for metals and alloys in hot working. Mater Des. 2011;32:1733–59.

49. Reyes-Calderon F, Mejıa I, Cabrera JM. Hot deformation activation energy (QHW) of austenitic Fe–22Mn–1.5Al–1.5Si–0.4C TWIP steels microalloyed with Nb, V, and Ti. Mater Sci Eng A. 2013;562:46–52.

50. Cabanas N, Penning J, Akdut N, Cooman BC. High-temperature deformation properties of austenitic Fe-Mn alloys. Metall Mater Trans A Phys. 2006;37:3305–15.

51. Zhao H, Qi J, Liu G, Su R, Sun Z. A comparative study on hot deformation behaviours of low-carbon and medium-carbon vanadium microalloyed steels. J Mater Res Technol. 2020;9(5):11319–31.

52. Jabłońska MB, Jasiak K, Kowalczyk K, Bednarczyk I, Skwarski M, Tkocz M, Gronostajski Z. Deformation behaviour of high-manganese steel with addition of niobium under quasi-static tensile loading. Mater Sci-Pol. 2022;40(3):1–11. https://doi.org/10.2478/msp-2022-0029.

Publisher's Note Springer Nature remains neutral with regard to jurisdictional claims in published maps and institutional affiliations.